

Comet 289P/Blanpain: Near-Perihelion Activity and the Phoenicids

TOSHIHIRO KASUGA¹

¹*National Astronomical Observatory of Japan, 2-21-1 Osawa, Mitaka, Tokyo 181-8588, Japan*

(Accepted for publication in The Astronomical Journal, 2024 November 19)

ABSTRACT

We present NEOWISE observations of Jupiter family comet 289P/Blanpain, the parent body of the Phoenicid meteoroid stream. Near-infrared images at $3.4\mu\text{m}$ ($W1$) and $4.6\mu\text{m}$ ($W2$) were obtained near perihelion on two occasions: UT 2019-10-30 (inbound, heliocentric distance $R_h = 1.20$ au) and UT 2020-01-11/12 (outbound, $R_h = 1.01$ au). To assess faint activity, we establish constraints on dust production driven by the limited sublimating area of water ice, based on studies of the 1956 Phoenicids. The ejected dust mass is $M_d = 4100 \pm 200$ kg (inbound) and 1700 ± 200 kg (outbound), respectively. The dust production rates are $Q_{\text{dust}} = 0.01 - 0.02$ kg s⁻¹, corresponding to dust-to-gas production ratio $2 \leq f_{\text{dg}} \leq 6$. The resulting fractional active area, $f_A = 3.8 \pm 1.9 \times 10^{-5}$, is the smallest yet reported. The absence of $4.6\mu\text{m}$ ($W2$) excess suggests that 289P contains negligible amounts of CO₂ and CO. Time-resolved analysis of weighted mean of $W1$ and $W2$ magnitudes finds a distinctive peak amplitude in the light curve having a rotational period $P_{\text{rot}} = 8.8536 \pm 0.3860$ hr, however, further verification is needed. The perihelion-normalized nongravitational acceleration, $\alpha'_{\text{NG}} = 3.1 \times 10^{-6}$, is approximately an order of magnitude smaller than the trend observed for well-studied comets, consistent with weak outgassing. Current dust production from 289P, regardless of plausible assumptions for particle size and distribution, is an order of magnitude too small to produce the Phoenicid stream within its ~ 300 year dynamical lifetime. This suggests another mass supply, probably in 1743–1819, rapid rotational destruction of a sub-km precursor body, resulting in fragments equaling the mass of an object with radius ~ 100 m.

Keywords: Small Solar System bodies (1469), Near-Earth objects (1092), Comets (280), Short period comets (1452), Asteroids (72), Meteors (1041), Meteor streams (1035), Meteor trails (1036), Space telescopes (1547), Infrared telescopes (794), Sky surveys (1464), Catalogs(205)

1. INTRODUCTION

Corresponding author: Toshihiro Kasuga
toshi.kasuga@nao.ac.jp

Comet 289P/Blanpain (hereafter 289P), formerly known as D/1819 W1, was discovered in 1819 November by J.-J. Blanpain (Kronk 2003)¹. The comet was subsequently linked to the Phoenicid meteor shower² as a potential parent body due to their orbital similarities (Ridley 1957; reviewed in Ridley 1963). Independent discovery and following observations were made for about two months until 1820 January. Throughout this period, the comet appeared small, faint and without a tail or gas. The orbit was determined to have a period of about 5 years (Jupiter-family type), placing 289P shortly after its perihelion at the time of observations. Nevertheless, it remained lost for nearly two centuries after these initial observations.

In 2003 November, the near-Earth asteroid (NEA) 2003 WY₂₅ was discovered by the Catalina Sky Survey (Ticha et al. 2003). The orbit has a semimajor axis $a = 3.045$ au, eccentricity $e = 0.685$, and inclination $i = 5^\circ.9$ (Epoch 2458746.5 (2019-Sep-20.0) from NASA JPL Small-Body Database Lookup, solved on 2024 July 26). The Tisserand parameter with respect to Jupiter, $T_J = 2.817$, is consistent with dynamical classification as a member of the Jupiter family comets (JFCs). Its orbital similarity to 289P, coupled with backward integrations of the 2003 WY₂₅ orbit, suggested that the two bodies might be same (Foglia et al. 2005; Micheli 2005).

Observations and recent dynamical studies of the Phoenicid meteor shower revealed the identification of 289P with 2003 WY₂₅. On 1956 December 5, the sudden outburst of the shower was observed both by visual and radio-echo in the Southern Hemisphere (Kronk 2014). Notably, J. Nakamura witnessed the most significant activity of the 1956 Phoenicid outburst (300 meteors per hour) on Soya, a Japanese expedition ship to the Antarctic, in the Indian Ocean (Huruhata & Nakamura 1957). Watanabe et al. (2005) applied dynamical study to 2003 WY₂₅ and its orbital elements in the context of dust trail theory (Asher 2000; Sato 2003) to estimate the conditions leading to the 1956 Phoenicids outburst. The result found that dust trails were formed and bundled between 1743 and 1808, with the 1760–1808 trails being particularly responsible for the event, leading to the conclusion that 2003 WY₂₅ is identical to 289P (Watanabe et al. 2005) (see also, Jenniskens & Lyttinen 2005; Jenniskens 2006).

Shortly thereafter, cometary activity in 289P was confirmed to be ongoing. In 2004 March, Jewitt (2006) optically observed 289P when at the heliocentric distance $R_h = 1.64$ au, finding a weak coma indicative of mass-loss rate of 0.01 kg s^{-1} and a small nucleus radius (r_n) of only 160 m^3 (an order of magnitude smaller than typical cometary nuclei). In 2013 July, an asymmetric coma and a tail were observed in 289P at the large $R_h = 3.88$ au, with a maximum V-band apparent magnitude of 17.5 (Williams et al. 2013). The limited mass-loss within the stream age ($\tau_s \sim 300$ yrs) is insufficient to explain the estimated mass of the Phoenicid stream, suggesting that the stream might be produced impulsively, perhaps by breakup of the precursor body (reviewed in Kasuga & Jewitt 2019).

The short dynamical age of the Phoenicid stream requires a substantial dust supply from 289P. Since JFCs and other type of comets typically exhibit their strongest mass-loss activity around their perihelia, we investigate the dust production rate of 289P near its perihelion ($q = 0.96$ au) to assess its potential contribution to the Phoenicid stream. The latest opportunity occurred from the end of 2019 to the beginning of 2020. We used data acquired by the *Near-Earth Object Wide-field Infrared Survey*

¹ <https://cometography.com/pcomets/1819w1.html>

² PHO/254 from IAU Meteor Data Center, Nomenclature (Jopek & Jenniskens 2011)

³ The uncertainty is estimated several tens of percent based on the probable linear phase function range (Jewitt 2006). In this study we assume the radius uncertainty of 25%, corresponding to $r_n = 160 \pm 40 \text{ m}$.

Explorer (NEOWISE, Mainzer et al. 2011, 2014) during both the inbound and outbound perihelion passages of comet 289P/Blanpain.

2. NEOWISE

This study is based on near-infrared data obtained by NEOWISE (Mainzer et al. 2011, 2014), the extended mission of WISE (Wright et al. 2010). Launched on 2009 December 14 into a Sun-synchronous polar orbit, WISE was equipped with a 40 cm telescope that employed beam splitters to simultaneously capture images at four infrared wavelength bands centered at $3.4\mu\text{m}$ ($W1$), $4.6\mu\text{m}$ ($W2$), $12\mu\text{m}$ ($W3$), and $22\mu\text{m}$ ($W4$), enabling a comprehensive all-sky survey. It started on 2010 January 7 and continued until 2010 September 29. As the cryogen reserve was exhausted, data acquisition terminated for $W3$ and $W4$. WISE further continued surveying in a post-cryogenic two-band survey mode until 2011 February 1, when it was placed in hibernation. The two-band survey ($W1$ and $W2$), subsequently named NEOWISE, resumed 2013 December 13 and continues as the NEOWISE-R reactivation project.

NEOWISE employs a 1024×1024 pixel HgCdTe focal-plane array detector (Teledyne Imaging Sensors) for both the $W1$ and $W2$ bands (Wright et al. 2010). The detector exhibits a pixel scale of $2''.75 \text{ pix}^{-1}$ and a field of view (FOV) of $47' \times 47'$. Consecutive pairs of frames, one for each band, are captured within the same FOV every 11 seconds, with each frame having an exposure time of 7.7 seconds. The NEOWISE mission data ($W1$ and $W2$ bands) are available through the NASA/IPAC Infrared Science Archive (IRSA⁴).

2.1. Data

We retrieved all detections of comet 289P/Blanpain using the IRSA search tools (GATOR⁵ and WISE Image Service⁶). The queried sources in the GATOR are NEOWISE-R Single Exposure (L1b) (NEOWISE Team 2020), WISE All-Sky Single Exposure (L1b) (WISE Team 2020a), WISE 3-Band Cryo Single Exposure (L1b) (WISE Team 2020b), and WISE Post-Cryo Single Exposure (L1b) (WISE Team 2020c). These detections were also verified using the WISE Image Service.

For this study, we conducted the data screening process following the methods of the NEOWISE Comet Team (Stevenson et al. 2015; Rosser et al. 2018; Bauer et al. 2021; Gicquel et al. 2023; Milewski et al. 2024). We applied the selection criteria for a moon angular separation $> 30^\circ$, and an angular distance from the nominal boundaries of the South Atlantic Anomaly (SAA) $> 0^\circ$. We selected observations having flags of `cc_flags = 0` which ensures no contamination produced by known artifacts, e.g. latent images or diffraction spikes (Mainzer et al. 2011). All scores in the profile-fit photometric quality flag (`ph_qual`) and the frame quality (`qual_frame`) were checked, given that cometary coma is extended and not always imaged as a point source. We visually inspected the single exposure frames collected above. An image of comet 289P was confirmed when its optical magnitude $< 22 \text{ mag}$, and data for this study were selected accordingly. Following Bauer et al. (2012), for objects detected at multiple epochs, we define a ‘‘Visit’’ as a set of observations separated by time and distinct sky regions. We found two observation epochs, Visit *A* (MJD 58786: UT 2019-10-30, inbound) and Visit *B* (MJD 58860: UT 2020-01-11/12, outbound), for 289P.

2.2. Single Exposure Image

⁴ <https://irsa.ipac.caltech.edu/frontpage/>

⁵ <https://irsa.ipac.caltech.edu/cgi-bin/Gator/nph-scan?submit=Select&projshort=WISE>

⁶ <https://irsa.ipac.caltech.edu/applications/wise/>

We measured the FWHM of the 289P image in single exposure frames, finding values of $5''.8\text{--}6''.6$ for $W1$ and $6''.3\text{--}8''.8$ for $W2$, respectively. These wider FWHM values, mostly beyond the nominal point-spread function (PSF) of $6''.0$ used in the GATOR photometry⁷, are indicative of an extended coma surrounding 289P. The nominal PSF is applied for point-like objects such as asteroids and stars, and the aperture radius for photometry is set $7''.5$ ($= 1.25 \times \text{FWHM}$). The short radius can not capture the entire extent of the emission of comets, leading to underestimation of the brightness of 289P. Therefore, to enclose the entire emission and improve the brightness measurements, we conducted photometry on the data selected using synthetic circular apertures projected onto the sky. The photometric aperture radius was set twice the FWHM in the image ($\approx 12''\text{--}18''$) and the sky background was determined within a concentric annulus having projected inner and outer radii of $30''$ and $45''$, respectively. This aperture radius is reasonable to active comets in the NEOWISE/WISE data for enclosing most of the light source (cf. $11''$ -radius, [Stevenson et al. 2015](#)). The sky range applied here was set smaller due to the low Signal-to-Noise Ratio (SNR) in the data, especially for $W1$. Images corrupted by stars, artifacts, or noise were excluded. Data with an extremely low SNR (< 1) were rejected. To mitigate star contamination, particularly prevalent in the shorter $W1$ band, images with $W1$ SNR $> W2$ SNR were removed. The stellar thermal signatures ($\gtrsim 2000$ K) have their blackbody peaks in the shorter wavelengths, leading to their appearances in these bands ([Kasuga & Masiero 2022](#)). This issue was found in the $W1$ band from Visit B (MJD 58860: 2020-01-11/12, outbound) (Section 3.1). There were no saturated images brighter than the threshold of $W1 = 8.1$ mag, $W2 = 6.7$ mag.

The measured instrumental source brightness (counts in digital numbers) was calibrated to magnitude by referring an instrumental zero point magnitude⁸ ([Cutri et al. 2012, 2015](#)). The magnitudes were converted to the flux density (Jy) using the published zero points ([Wright et al. 2010](#)), and no color corrections were applied for 289P (e.g. [Bauer et al. 2021](#)). We followed the photometry and calibration methodology on the IRSA website⁹ ([Cutri et al. 2012, 2015](#)) as appropriate. The observation log and photometric results are shown in Table 1. The orbital information is summarized in Table 2.

2.3. Composite Image

We created coadded images from both Visit A and B using the Image Co-addition with Optional Resolution Enhancement (ICORE) ([Masci 2013](#))¹⁰. ICORE combines the data frames into a single averaged image, resamples the original NEOWISE (WISE) single-exposure frames, and convolves the mosaic pixel with the original PSF. The system extracts target object positions (RA and DEC) from individual images and repositions the corresponding image cutouts, assigning the recentered positions to the provided RA and Dec. The orientation of the coadded images is then adjusted to align North up and East to the left. In this study, the image size is set at $277'' \times 277''$ (0.077 deg \times 0.077 deg). The resulting coadded images have a resampled pixel scale of $1''.0 \text{ pix}^{-1}$, down from $2''.75 \text{ pix}^{-1}$.

The ICORE processed both data in the Visits A and B to create composite images. The $W2$ image from Visit B had a small, cavity-like artifact on the 289P image. We hesitated to conduct a cleaning process on the comet image. Then we alternatively applied a median-combination process

⁷ https://wise2.ipac.caltech.edu/docs/release/allsky/expsup/sec4_4c.html

⁸ https://wise2.ipac.caltech.edu/docs/release/allsky/expsup/sec4_4h.html#CalibratedM

⁹ https://wise2.ipac.caltech.edu/docs/release/allsky/expsup/sec4_4h.html

¹⁰ <https://irsa.ipac.caltech.edu/applications/ICORE/>

using *IRAF* for the Visit *B* dataset. This is because the ICORE package applies area-averaged image combine process (Equation (10) in Section 7)¹¹. In contrast, a clipped median combination (which rejects the extreme pixel data values before computing the median of the remainder) can suppress artifacts, noise and background structures (Jewitt et al. 2020). This approach is effective for Visit *B* since 289P is imaged in a sky region where faint stars are densely packed. Visit *B* obtained two single-exposure frames taken at $\Delta = 0.09$ au, both with sufficient SNR ~ 25 for the combination process using *IRAF*. The orientation of each image was rotated to bring the direction of the position angle to north at the top and east at the left, and they were shifted to align the images using fifth-order polynomial interpolation. The images were then median-combined into a single image, maintaining a pixel scale of $2''.75 \text{ pix}^{-1}$.

Figures 1 and 2 show the ICORE coadded and median-combined images for Visit *A* and *B*, respectively. Photometry was conducted using the aperture radius twice the FWHM in the image ($\approx 12'' \sim 18''$) and the sky background was determined within a concentric annulus having projected inner and outer radii of $40''$ and $55''$, respectively. The results are shown in Table 3.

3. ANALYSIS

3.1. Surface Brightness

The Visit *B* composite images (median-combined) captured both 289P and nearby field stars simultaneously. For comparison, we measured the surface brightness profiles of both in the *W1* and *W2* bands. The surface brightness, as a function of the angular radius, was obtained using concentric annular apertures with a width of $2''.75$ ($= 1 \text{ pix}$) extending to a radius of $100''$ ($= 36 \text{ pix}$). Figures 3 and 4 show the profiles in the *W1* and *W2* bands, respectively.

Figure 3 shows that the *W1* profiles are broader profile compared to a field star. However, beyond 15 pixels ($\sim 41''$), the profile of 289P becomes severely influenced by the uneven structure from the background (Section 2.2). This effect renders the data unsuitable for further profile analysis. On the other hand, Figure 4 shows that the *W2* profile for 289P is similar to that of a field star, with a slightly broader extension towards the edge of the wings. We have a short note that these surface brightness profiles cannot provide constraints on the activity levels of 289P. As an example, the FWHM of 289P in the *W2* band is $\theta_F = 6''.9$, which is $\sim 8\%$ larger than the NEOWISE/WISE angular resolution of $6''.4$ (*W2*) ($6''.1$ for *W1*, Wright et al. 2010)¹². Therefore we can only compare the profile of 289P to those of the field stars.

Alternatively, the profiles allow to constrain the speed of dust ejection from 289P. The profiles and visual checks of the NEOWISE data revealed almost no discernible coma, suggesting a compact and faint dust distribution in 289P (Jewitt 1991, 2006). The weak or absence of a coma is a clear indicator of the extremely low velocities at which dust particles are ejected from 289P, as in the case of main-belt comet 133P/Elst-Pizarro (Jewitt et al. 2014). We estimated the velocities of ejected dust, v_d , using turnaround distance of particles toward the Sun, with the equation $X_R = v_d^2 / (2\beta g_\odot)$ (Jewitt & Meech 1987). The dimensionless parameter β , relates to particle radius as $\beta \sim 1/a_{\mu\text{m}}$ (Bohren & Huffman 1983), where $a_{\mu\text{m}}$ is the particle radius expressed in microns. Then we obtain a constant for dust particles ejected from the 289P nucleus (Jewitt et al. 2014),

$$v_d^2 a_{\mu\text{m}} = 2 g_\odot X_R, \quad (1)$$

¹¹ <https://irsa.ipac.caltech.edu/applications/ICORE/docs/icore.pdf>

¹² <https://wise2.ipac.caltech.edu/docs/release/prelim/>

in which g_{\odot} is the solar gravitational acceleration expressed as $g_{\odot} = GM_{\odot}/R_{\text{h}}^2$, where $G = 6.67 \times 10^{-11} \text{ m}^3 \text{ kg}^{-1} \text{ s}^{-2}$ is the gravitational constant, $M_{\odot} = 2 \times 10^{30} \text{ kg}$ is the mass of the Sun, and R_{h} is expressed in meters. We apply the *W2* composite data from Visit *B*, and substitute $X_{\text{R}} < 450 \text{ km}$ ($\theta_{\text{F}} = 6''.9$ at $\Delta = 0.09 \text{ au}$) and $g_{\odot} = 5.8 \times 10^{-3} \text{ m s}^{-2}$ at $R_{\text{h}} = 1.01 \text{ au}$ to find $v_{\text{d}}^2 a_{\mu\text{m}} < 5200 \text{ m}^2 \text{ s}^{-2}$. For example, with $a_{\mu\text{m}} = 2.3$, half the *W2* wavelength (Bauer et al. 2011), we find $v_{\text{d}} < 48 \text{ m s}^{-1}$. For a millimeter-radius particle ($a_{\mu\text{m}} = 1000$), we find 2.3 m s^{-1} . These derived dust velocities are significantly lower than those calculated for thermal gas outflows in active comets with the similar R_{h} . As a preliminary estimate, the Whipple model (Whipple 1951) predicts that the μm -sized particles, likely coupled to the outflowing gas (Harmon et al. 2004), have speeds $v_{\text{d}} = 260 \text{ m s}^{-1}$ from 289P. Thermal gas, on the other hand, is expected to reach velocities $v_{\text{g}} = 570 \text{ m s}^{-1}$ at $R_{\text{h}} \sim 1 \text{ au}$ with temperature $T \sim 278 \text{ K}$ (Equation (10) of Graykowski & Jewitt 2019). However, these calculated values are more than five times larger than the inferred values from the 289P profile. The absence of distinct coma further suggests low dust ejection velocities due to the weak activity of 289P.

3.2. Sublimation from Ice Patch

The small source approximation (SSA) model (Jewitt et al. 2014) provides a framework for investigating the mechanism responsible for the slow ejection of dust particles. We apply this model to estimate water ice sublimation from a small surface patch on comet 289P. The radius of ice sublimating patch, r_{s} , is given by (Equation (A5) of Jewitt et al. 2014),

$$r_{\text{s}} = \frac{4\rho_{\text{d}}a_{\text{d}}}{3C_{\text{D}}v_{\text{g}}F_{\text{s}}} \left(v_{\text{d}}^2 + \frac{8\pi G\rho_{\text{n}}r_{\text{n}}^2}{3} \right), \quad (2)$$

where ρ_{d} is the bulk density of dust, a_{d} is radius of dust particle, $C_{\text{D}} \sim 1$ is a dimensionless drag coefficient which depends on the shape and porosity of the grain, v_{g} is the thermal velocity of gas molecules, F_{s} is the specific mass-loss rate of ice sublimation, v_{d} is the terminal ejection velocity of dust, G is the gravitational constant, ρ_{n} is the bulk density of comet nucleus, r_{n} is the radius of comet 289P. We assume the same bulk density for dust and nucleus, $\rho_{\text{d}} = \rho_{\text{n}} = 1000 \text{ kg m}^{-3}$, as used in the prior study of 289P (Jewitt 2006). The energy balance equation for an ice patch exposed at the subsolar point calculates $F_{\text{s}} = 3.2 \times 10^{-4} \text{ kg m}^{-2} \text{ s}^{-1}$ with $T = 200 \text{ K}$ in Visit *A* and $4.7 \times 10^{-4} \text{ kg m}^{-2} \text{ s}^{-1}$ with $T = 202 \text{ K}$ in Visit *B*, respectively (Equation (6) of Kasuga & Jewitt 2015). Furthermore, we employ the following values, $v_{\text{g}} \sim 480 \text{ m s}^{-1}$ ($T \sim 200 \text{ K}$ at $R_{\text{h}} = 1.01\text{--}1.20 \text{ au}$) and $r_{\text{n}} = 160 \pm 40 \text{ m}$ (Jewitt 2006). The values of r_{s} , a_{d} and v_{d} remain unknown.

The 1956 Phoenicids can constrain the parameters of dust particle size and ejection velocity. The eyewitness accounts (Huruhata & Nakamura 1957, and private communication with J. Nakamura) indicate that the Phoenicid meteoroids had apparent magnitudes brighter than approximately $+6.0 \sim +6.5 \text{ mag}$ and the corresponding mass is $> 10^{-6} \text{ kg}$ (Table I in Lindblad 1987; Kronk 2014). With the assumed $\rho_{\text{d}} = 1000 \text{ kg m}^{-3}$, the corresponding radius of the dust particle (meteoroid) is $\gtrsim 1 \text{ mm}$. The dynamical study found that the 1956 Phoenicids primarily originated from the dense trails produced between 1760 and 1808, with slow dust ejection velocities, $0.49 \leq v_{\text{d}} \leq 0.73 \text{ m s}^{-1}$ (see Table 1 in Watanabe et al. 2005).¹³ Substituting $a_{\text{d}} \sim 1 \text{ mm}$ (as the lower limit) and $v_{\text{d}} \sim 0.5 \text{ m s}^{-1}$ (median value of those computed) into Equation (2) yields $1.6 \pm 0.1 \text{ m} \leq r_{\text{s}} \leq 2.3 \pm 0.1 \text{ m}$. With

¹³ The 1760–1808 period encompasses dust trails ejected from the parent body in 1760, 1766, 1771, 1776, 1782, 1787, 1792, 1797, 1803, and 1808. Dust particle sizes used in the simulation were insensitive to radiation pressure, corresponding to millimeter-scale (Watanabe et al. 2005).

the determined r_s (≈ 2 m), the ejection velocity of dust (v_d) is calculated as a function of particle radius (a_d) using Equation (2). The comparison of the SSA and Whipple models, both applied to 289P, is shown in Figure 5. The limit for dust particle of $a_d = 2.3 \mu\text{m}$ with $v_d < 48 \text{ m s}^{-1}$, which is measured from the FWHM of 289P (*W2*) in 2020 (Visit B) (Section 3.1), is shown in the same Figure. The dust velocity is about five times larger than the calculated velocity by the SSA model. Substituting $a_d = 2.3 \mu\text{m}$, $v_d < 48 \text{ m s}^{-1}$ and the same parameters above (Visit B) into Equation (2), we find $r_s \lesssim 31$ m. The straightforward interpretation is that the ice patch area on the comet surface might have enlarged since 1760–1808. However, we have a note on the spatial resolution of the data. NEOWISE’s limited resolution, with a pixel scale of $2''.75 \text{ pix}^{-1}$, results in low angular resolution (Section 2). By comparison, for example, the Very Large Telescope (VLT) VISIR has a high resolution of $\sim 0''.05 \text{ pix}^{-1}$ in the mid-infrared wavelengths (Jewitt et al. 2019). The resolution gap is 180 km pix^{-1} (NEOWISE) versus 3 km pix^{-1} (VLT) at the distance of 289P in Visit B ($\Delta=0.09$ au). Thus, the measured dust velocity by NEOWISE ($v_d < 48 \text{ m s}^{-1}$) would be an overestimate and should be considered an upper limit. The corresponding radius of ice patch ($r_s \lesssim 31$ m) is considered likewise. Higher spatial resolution observations would improve estimates of dust velocity and ice patch area. Such data would allow us to constrain the long-term stability of 289P’s surface ice source regions and its overall activity.

The radius of ice sublimating patch, r_s , is related to the critical radius of dust particles to be launched, a_c , using Equation (A6) in Jewitt et al. (2014),

$$a_c \lesssim \frac{9C_D v_g F_s r_s}{32\pi G \rho_n \rho_d r_n^2}. \quad (3)$$

Substituting the above parameters, we find that the critical radius of dust particle to be ejected is $a_c \lesssim 2$ cm. This size is consistent with relatively large meteoroids which are typically seen as fireballs (Lindblad 1987). Actually, J. Nakamura observed bright, fireball-class Phoenicids too during its peak activity period (Huruhata & Nakamura 1957), as noted by Watanabe et al. (2005). The estimated critical particle size is consistent with the observational result of the Phoenicids.

3.3. Rotation Period

Comet 289P/Blanpain likely exhibits weak activity driven by ice sublimation. While it is very subtle, the outgassing might corrupt the strict periodicity of the nucleus light curve (Jewitt 1991). Nevertheless, Visit A provides consecutive datasets of brightness to search for the rotation period of 289P (Table 1). We applied spectral analysis using the Discrete Fourier Transform (DFT) algorithm (Lomb 1976; Scargle 1982) to the time-series data acquired in the *W1* and *W2*, respectively. This method employs a significance level to assess the quality of the fit at a given period, using spectral power as a function of angular frequency. The highest significance level corresponds to maximum power at the frequency, indicating the most convincing solution for the periodicity. The light curve was assumed to be a double-peaked shape, as commonly observed in elongated small bodies in the solar system. Then we searched the rotational period, P_{rot} , using the uncertainty estimation equation given by Gilliland & Fisher (1985) (Equation (7) in Kasuga & Jewitt 2015) and we found $P_{\text{rot}} = 15 \pm 3$ hr in the *W1* band and $P_{\text{rot}} = 13 \pm 2$ hr in the *W2* band, respectively. The phased light curve for each band is shown in Figures 6 and 7. The *W1* light curve (Figure 6) shows low SNR and unclear systematic variations, with large photometric uncertainties relative to its amplitude range. In contrast, the *W2* light curve (Figure 7) shows moderate SNR but shows an inconsistent shape

compared to the $W1$ light curve. Both rotational periods are determined with a significance level of $\sim 45\%$.

To find a better constraint on the rotational period, we used a weighted mean of the $W1$ and $W2$ magnitudes. Missing data points in Table 1 were interpolated and extrapolated, assuming uncertainties of 0.3 mag and 0.2 mag for $W1$ and $W2$, respectively. The calculated weighted mean, W_{wm} , is presented in Table 4. By fitting W_{wm} , we identify a primary rotational period, $P_{\text{rot}} = 8.8536 \pm 0.3860$ hr, with a significance level of 30.5%. The phased light curve and significance level are shown in Figure 8. A secondary candidate period, $P_{\text{rot}} \sim 15.6$ hr (~ 0.65 day), with a similar significance level of 30.4%, was also identified, consistent with individual band analysis. Light curves with periods around $P_{\text{rot}} \sim 13 - 15$ hr exhibit a typical double-peak pattern with similar amplitudes (Figures 6 and 7). However, Figure 8 (left panel) reveals a distinctive peak in the amplitude curve at a phase ~ 0.6 . This peak might indicate an active spot on the 289P surface. In some observed active comets, the rotation period of the nucleus can be inferred from periodic structures, like jets and spirals (localized activities), in the coma, even when the nucleus is too faint for photometric isolation (Samarasinha & A’Hearn 1991; Samarasinha et al. 2004), as noted by Jewitt (2021). From this perspective, we adopt $P_{\text{rot}} = 8.8536 \pm 0.3860$ hr as the principal rotational period of 289P.

We have a note that the derived low significance levels of $\sim 30 - 45\%$ indicate high uncertainties in the determined periods. For comparison, the rotational periods of the dormant JFC 169P/NEAT (Figure 3 in Kasuga et al. 2010) and NEA 2003 EH₁ (Kasuga & Jewitt 2015) were determined with a significance level exceeding $\gtrsim 99\%$, corresponding to the maximum power in the spectral analysis. The resulting uncertainties of these periods were $\lesssim 0.01$ hr, more than an order of magnitude smaller than those of 289P. Thus, the obtained light curves for 289P may not be entirely reliable due to the low SNR and the limited number of data points.

On the contrary, the fitted light curve models may indicate the presence of an expanded coma. Assuming the variations originated solely from the nucleus rotation, the maximum photometric range would be $\Delta m_w = 1.3 \sim 2.0$ (Figures 6, 7, and 8). This value can be used to derive a lower limit to the intrinsic axis ratio, b/c , between long axis b and short axis c . Assuming its perpendicular rotation (the rotational axis is perpendicular to our line of sight), the equation, $b/c = 10^{0.4\Delta m_w}$, gives the ratio $b/c \sim 3.3 - 6.3$. This derived intrinsic axis ratio suggests a highly elongated shape, far exceeding those observed in typical km-sized cometary nuclei ($b/c \geq 1.5$; Jewitt 2004) (see also, Kokotanekova et al. 2017; Knight et al. 2023). Substituting $b/c \sim 3.3 - 6.3$ and $P_{\text{rot}} \sim 8.8536$ hr into Equation (4) of Jewitt & Li (2010), we find the critical bulk density $1500 - 5500$ kg m⁻³. This uncertainty is extremely large. Given the current data, further interpretation is not justified due to probable contamination from the coma.

3.4. Flux Model: Reflected Sunlight and Thermal Emission

Generally, active comets detected by NEOWISE are composed of reflected sunlight, gas (CO₂ and CO) and thermal emissions. Reflected sunlight is observed in the $W1$ band, attributed to light scattering by cometary dust particles. The gas and thermal emissions are observed in the $W2$ band and at longer wavelengths (Bauer et al. 2015). However, the presence of CO₂ and CO is not confirmed in 289P (discussed in Section 4.2). In this section, we present the models for 289P applied to reflected sunlight and thermal emission.

For active comets with comae, the flux density, F_ν , is a combination of reflected sunlight, F_ν^{Ref} , and thermal emission, F_ν^{IR} , primarily from dust particles. The equation is expressed as

$$F_\nu = F_\nu^{\text{Ref}} + F_\nu^{\text{IR}}. \quad (4)$$

In which F_ν^{Ref} (Jy) is calculated by correcting the Sun-observer-object distance using the equation

$$F_\nu^{\text{Ref}} = \frac{\pi B_\nu(T_\odot) R_\odot^2}{R_h^2} A \pi \left(\frac{D_e}{2}\right)^2 \frac{\Phi_{\text{HM}}(\alpha)}{\Delta^2}, \quad (5)$$

where B_ν is the Planck function (Jy sr^{-1}) at the Solar temperature $T_\odot = 5778 \text{ K}$, $R_\odot = 6.957 \times 10^{10} \text{ cm}$ is the Solar radius, R_h is heliocentric distance (cm). The $A \approx A_v = p_v q_p$ is the bolometric Bond albedo, where p_v is the visible geometric albedo and q_p is the phase integral. We assume $p_v = 0.04$ as typical of the nuclei of short-period comets with low- T_J (Lamy et al. 2004; Fernández et al. 2013) and $q_p = 0.30$, based on measurements for the short-period JFCs by telescopes (Fernández et al. 2003; Buratti et al. 2004) and spacecraft ($q_p \sim 0.20\text{--}0.30$, Knight et al. 2023). D_e is the effective diameter of a circle whose area is equal to the combined area of all the dust particles and nucleus (cm). $\Phi_{\text{HM}}(\alpha)$ is the Halley-Marcus composite phase function for scattered sunlight by dust particles in cometary comae (Schleicher et al. 1998; Marcus 2007) in which α is the phase angle (in degrees), and Δ is the *WISE*-centric distance (cm). In Equation (4), F_ν^{IR} (Jy) is calculated by

$$F_\nu^{\text{IR}} = \epsilon \left(\frac{D_e}{2}\right)^2 \frac{B_\nu(T_d)}{\Delta^2} \quad (6)$$

where $\epsilon = 0.9$ is the infrared emissivity for the typical value measured from silicate powders (Hovis & Callahan 1966; Lebofsky et al. 1986), $B_\nu(T_d)$ is the Planck function (Jy sr^{-1}) at the dust temperature, T_d (Kelvin). D_e (cm) and Δ (cm) are the same in Equation (5). The cometary dust temperature, T_d , is empirically adopted as approximately 3% warmer than the blackbody temperature, $T_{\text{bb}} = 278 \times R_h^{-1/2}$ (kelvin), yielding $T_d \approx 1.03 \times T_{\text{bb}}$ (Stevenson et al. 2015). These models were applied to the composite image measurements (Table 3). As for the observing geometry, we used those of median values in Table 1: $R_h = 1.20 \text{ au}$, $\Delta = 0.40 \text{ au}$ and $\alpha = 49.8^\circ$ for Visit *A*, and $R_h = 1.01 \text{ au}$, $\Delta = 0.09 \text{ au}$ and $\alpha = 70.2^\circ$ for Visit *B*, respectively. Using Equation (4), we conducted least-square fits to the measured flux densities in Table 3: $W1 = 1.35 \pm 0.17 \times 10^{-4} \text{ Jy}$ and $W2 = 1.05 \pm 0.06 \times 10^{-3} \text{ Jy}$ for Visit *A*, and $W1 = 3.02 \pm 0.13 \times 10^{-3} \text{ Jy}$ and $W2 = 2.24 \pm 0.08 \times 10^{-2} \text{ Jy}$ for Visit *B*, respectively. Then, we obtain D_e . The results are shown in Table 5. The modeled spectral energy distributions and measured flux densities for Visits *A* and *B* are shown in Figures 9 and 10, respectively. The obtained values, $D_e = 1.43 \pm 0.04 \text{ km}$ for Visit *A* ($R_h = 1.20 \text{ au}$) and $D_e = 0.96 \pm 0.01 \text{ km}$ for Visit *B* ($R_h = 1.01 \text{ au}$), are consistent within a factor of two, indicating the stable near-perihelion activity during both Visits (confirmed in Section 4.1).

We have a short technical note on model fitting. To ensure a meaningful least-square fit, we employed a single free parameter (D_e) in the model. Including geometric albedo (p_v) as an additional free parameter would create an overdetermined system with exactly two observed data points ($W1$ and $W2$) and two free parameters (D_e and p_v). This leads to zero degrees of freedom ($2 - 2 = 0$), potentially underestimating the uncertainties in the derived parameters. To estimate dust production rates in the next section, D_e and its uncertainty are focused.

4. RESULTS

The NEOWISE images present an indistinct coma in 289P. Active comets can be analyzed using the signals in the $W1$ and $W2$ bands to estimate the dust production rate and production rates of gases like CO_2 and CO , as demonstrated in previous studies (Bauer et al. 2008, 2011, 2015, 2021). In this section, we derive the dust production rate from 289P in Visits A and B , respectively, and explore the potential reasons for the lack of detectable gas emission.

4.1. Dust Production Rate: $W1$

We estimate the dust production rate using two methods. One uses the scattering cross-section of dust particles from coma in 289P. Another uses the $Af\rho$ -method (A'Hearn et al. 1984), similar to methods applied to comets observed by NEOWISE (Bauer et al. 2008, 2011, 2021; Milewski et al. 2024). These two results are compared for verification.

The cross-section of all the dust particles, C_d , is obtained by subtracting the nucleus cross-section of 289P, C_n , from the total cross-section, C_e (which includes contributions both from dust and nucleus): $C_d = C_e - C_n$. The total cross-section (C_e) and nucleus cross-section (C_n) are calculated using $C_e = \pi D_e^2/4$ (where D_e is from Table 5) and $C_n = \pi r_n^2$ (where $r_n = 160 \pm 40$ m), respectively. Then the ejected dust mass, M_d , is estimated by

$$M_d = \frac{4}{3} a_d \rho_d C_d, \quad (7)$$

where $a_d = 2.0 \mu\text{m}$ (half the median of the $W1$ and $W2$ wavelengths, adjusted from Bauer et al. 2011) is the radius of the dust particle contributing to dust coma brightness and $\rho_d = 1000 \text{ kg m}^{-3}$ is the assumed bulk density. For the particle radius modification ($a_d = 2.0 \mu\text{m}$), this is because D_e was determined by both $W1$ and $W2$ bands (Section 3.4), resulting in a slight adjustment to the particle radius from the originally applied value of $1.7 \mu\text{m}$. The residence time, τ , within the photometry aperture is estimated by $\tau = \rho/v_d$, where ρ is the radius of the aperture projected to the distance of the comet ($= 2 \times \text{FWHM}$ at Δ in Table 1) and $v_d = 11.5 \text{ m s}^{-1}$ (for $a_d = 2.0 \mu\text{m}$) is the dust ejection velocity calculated from Equation (2). The dust production rate, Q_{dust} (kg s^{-1}), is given by

$$Q_{\text{dust}} = \frac{M_d}{\tau} = \frac{4 a_d \rho_d C_d v_d}{3 \rho}. \quad (8)$$

The results (Q_{dust}), including C_d and M_d , are shown in Table 5. We obtain $Q_{\text{dust}} = 1.0 \pm 0.1 \times 10^{-2} \text{ kg s}^{-1}$ in Visit A ($R_h = 1.20$ au) and $Q_{\text{dust}} = 2.0 \pm 0.3 \times 10^{-2}$ in Visit B ($R_h = 1.01$ au), respectively, as it orbits around perihelion ($q = 0.96$ au). This low-level activity is consistent with the previous optical observation, $Q_{\text{dust}} \sim 0.01 \text{ kg s}^{-1}$ at $R_h = 1.64$ au in 2004 (Jewitt 2006).

Next, we applied the $Af\rho$ -method (A'Hearn et al. 1984). The parameter, $Af\rho$ (cm), is given by

$$\begin{aligned} Af\rho &= \frac{A(\alpha) f \rho}{\Phi_{\text{HM}}(\alpha)} \\ &= \frac{(2R_{\text{au}}\Delta)^2}{\Phi_{\text{HM}}(\alpha) \rho} 10^{(W1_{\odot} - W1)}, \end{aligned} \quad (9)$$

where A is the phase angle(α)-corrected albedo of the dust which equals to $A(\alpha)/\Phi_{\text{HM}}(\alpha)$ (Blaauw et al. 2014), f is the filling factor of the dust, $\Phi_{\text{HM}}(\alpha)$ is again the Halley-Marcus composite phase function, ρ is the radius of the aperture projected to the distance of the comet (the

same above), R_{au} is the heliocentric distance expressed in au, Δ is the WISE-centric distance in cm, $W1$ is the measured magnitude at $W1$ of 289P from the composite image, and $W1_{\odot}$ is the solar magnitude in the $W1$ band. Substituting the $W1$ values from Table 3 (15.903 ± 0.133 mag in Visit A and 12.525 ± 0.046 mag in Visit B , respectively) and $W1_{\odot} = -28.31$ mag¹⁴ into Equation (9), we find $Af\rho = 2.9 \pm 0.4$ cm in Visit A and $Af\rho = 10.6 \pm 0.4$ cm in Visit B , respectively. These $Af\rho$ can be converted to the dust production rate in kg s^{-1} , $Q_{Af\rho}$, using Cremonese et al. (2020) (see also, Fulle 2004),

$$Q_{Af\rho} \approx (Af\rho) \frac{2 a_d \rho_d v_d}{3 p_v}. \quad (10)$$

We adopt the same values of a_d , ρ_d , v_d and p_v as above. The results of the $Af\rho$ -method ($Q_{Af\rho}$) are also shown in Table 5. We obtain $Q_{Af\rho} = 1.0 \pm 0.2 \times 10^{-2} \text{ kg s}^{-1}$ in Visit A ($R_h = 1.20$ au) and $Q_{Af\rho} = 4.0 \pm 0.2 \times 10^{-2}$ in Visit B ($R_h = 1.01$ au), respectively.

Q_{dust} and $Q_{Af\rho}$ show consistency in Visit A , while in Visit B they show a difference by a factor of two. This difference in Visit B could be caused due to a few reasons. One is by inapplicability of the Halley-Marcus phase function (Φ_{HM}) at larger phase angles. Visit A had a phase angle $\alpha \sim 50^\circ$, while in Visit B it had a larger $\alpha \sim 70^\circ$. The Halley-Marcus is a composite function, having a critical point at $\alpha = 55^\circ$. It combines the use of the Halley-function at smaller phase angles (Schleicher et al. 1998) with the Marcus-function at larger angles (Marcus 2007)¹⁵ (see also, Marschall et al. 2022). This might influence the $Af\rho$ -method for deriving dust production rate as seen in Equations (9) and (10). Another cause could be the phase angle dependence of the dust velocities. The simulation conducted for JFC 67P/Churyumov-Gerasimenko (when at $R_h = 1.24$ au) finds that the speed of μm -sized dust particles at $\alpha \sim 70^\circ$ reaches only $\sim 80\%$ of those at $\alpha \sim 50^\circ$ (Figure 8, right panel in Agarwal et al. 2023). This slower speed at higher phase angle could influence the both methods, potentially overestimating the current production rates. For Visit B , we attempted to adopt $\sim 80\%$ of v_d in Visit A , which is $v_d = 9.2 \text{ m s}^{-1}$, finding $Q_{\text{dust}} = 2.0 \pm 0.1 \times 10^{-2} \text{ kg s}^{-1}$ and $Q_{Af\rho} = 3.0 \pm 0.1 \times 10^{-2} \text{ kg s}^{-1}$, respectively. The difference is mitigated by the 25% reduced value of $Q_{Af\rho}$. This is a preliminary analysis, implying the need for more precise calculations. However, it finds that the cross-section method is less sensitive to phase angle variations in this case. The comparison between Q_{dust} and $Q_{Af\rho}$ confirms that both methods can yield similar estimates, typically within a factor of a few.

The dust-to-gas production ratio, f_{dg} , is derived using (Jewitt et al. 2014),

$$f_{\text{dg}} = \frac{Q_{\text{dust}}}{\pi r_s^2 F_s}, \quad (11)$$

where r_s is the effective radius of the sublimating ice patch area, F_s ($\text{kg m}^{-2} \text{ s}^{-1}$) is the calculated specific mass-loss rate, and Q_{dust} (kg s^{-1}) is the measured dust production rate obtained above. Substituting the values derived in the previous sections for r_s , F_s and Q_{dust} yields $2 \leq f_{\text{dg}} \leq 6$ (approximated from $1.9 \pm 0.2 \leq f_{\text{dg}} \leq 5.6 \pm 1.0$). This result is comparable with measurements from 67P, where Rosetta found $f_{\text{dg}} = 4 \pm 2$ or ~ 6 (Rotundi et al. 2015; Fulle et al. 2016). 2P/Encke, the parent body of the Taurid meteoroid stream, has $10 \leq f_{\text{dg}} \leq 30$ (Reach et al. 2000).

¹⁴ <https://mips.as.arizona.edu/~cnaw/sun.html>

¹⁵ <https://asteroid.lowell.edu/comet/dustphase/details>

The fraction of active area (ice patch) on the nucleus surface, f_A , is derived using [Luu & Jewitt \(1992\)](#),

$$f_A = \frac{Q_{\text{dust}}}{4\pi r_n^2 f_{\text{dg}} F_s}. \quad (12)$$

Using the above parameters, we find $f_A \sim 5.1 \times 10^{-5}$ in Visit *A* and $f_A \sim 2.4 \times 10^{-5}$ in Visit *B*, respectively. Figure 11 shows the radius (m) versus fractional active area f_A for 289P, along with determinations of f_A for other JFCs ([Tancredi et al. 2006](#); [Kasuga et al. 2010](#)). The small active surface fraction of 289P is obvious, with the averaged value $f_A = 3.8 \pm 1.9 \times 10^{-5}$, compared to the km-sized JFCs. The similar small fraction ($f_A < 10^{-4}$) is found in 169P/NEAT, which remained in its dormant state even at $R_h = 1.4$ au ([Kasuga et al. 2010](#)). Small f_A is also found in 28P/Neujmin ($f_A = 0.001$), likely caused by dust mantle smothering the active area due to the gravity of its large 10 km radius body ([Tancredi et al. 2006](#)). The values $f_A > 1$ are seen in 21P/Giacobini-Zinner, 24P/Schaumasse and 73P/Schwassmann-Wachmann, indicating ice sublimation both from the nucleus and from icy grains ejected from nucleus ([Jewitt 2022](#)). The earlier study suggests that as nucleus radius decreases, f_A approaches unity on sub-km short-period comets, but selection bias possibly remains ([Jewitt et al. 2021](#)). Obtaining more samples for 100 m-sized bodies would be helpful while, 289P currently exhibits the smallest f_A among the reported JFCs.

4.2. Gas (CO_2 and CO) Production Rate: *W2*

The *W2* ($4.6\mu\text{m}$)-band is utilized for investigating the volatile compositions of active comets. Excess flux density in this band is interpreted as arising from the emission of gas molecules, primarily the CO_2 ν_3 vibrational fundamental band ($4.26\mu\text{m}$) and the CO $v(1-0)$ rovibrational fundamental bands ($4.67\mu\text{m}$). These volatile species have low sublimation temperatures of 20–100 K and are preserved in frozen ices or trapped as gases within the cometary nuclei, preferably at distant place beyond $R_h > 3$ au ([Priyalnik et al. 2004](#); [Womack et al. 2017](#); [Bouziani & Jewitt 2022](#)). Space-based imaging studies have placed the upper limits on those of production rates in active comets with $R_h \lesssim 12$ au ([Pittichová et al. 2008](#); [Bauer et al. 2011, 2015](#); [Stevenson et al. 2015](#); [Bauer et al. 2021](#); [Rosser et al. 2018](#); [Gicquel et al. 2023](#); [Milewski et al. 2024](#)). The individual gas emission bands, particularly those of CO_2 , have been detected in comets using satellite spectroscopy ([Ootsubo et al. 2012](#)).

However, we find no excess signal in 289P after removing reflected sunlight and thermal emission (Section 3.4). This indicates that CO_2 and CO gas production is negligibly small or absent in 289P. The small nucleus size ($r_n \sim 160$ m), the small $q = 0.96$ au, and the short $P_{\text{orb}} = 5.3$ yr likely drive its rapid sublimation and loss of CO_2 and CO . The core temperature around the 289P orbit (Equation (4) of [Jewitt & Hsieh 2006](#)) is $T_{\text{core}} \sim 180$ K. Even assuming a highly porous nature for 289P, similar to 67P, and a low thermal diffusivity $\kappa \sim 10^{-8} - 10^{-7} \text{ m}^2 \text{ s}^{-1}$ (from Rosetta, Appendix A), the longest timescale for heat diffusion into the core is $\tau_c \sim 8 \times 10^{3-4}$ yr. This suggests that solar heat can reach into the body core much sooner than the end of the dynamical lifetime of short-period comets $\sim 5 \times 10^5$ yr ([Duncan et al. 2004](#)). Consequently, CO_2 and CO are unlikely to be preserved, and mostly lost within the 289P nucleus.

Note that water-ice (H_2O) can still be contained in comet 289P. While the T_{core} exceeds the calculated sublimation temperature of pure water-ice 150 K ([Yamamoto 1985](#)), it is comparable to or lower than 180 K \sim 210 K range reported for dust-mixed water-ice ($f_{\text{dg}} = 3$) based on surface spectroscopic data of JFC 103P/Hartley 2 (EPOXI, [Yue et al. 2023](#)). This suggests that dust-mixed water ice within 289P ($2 \leq f_{\text{dg}} \leq 6$) would be more stable than pure ice, potentially hindering rapid

sublimation of water ice. The observed sublimation-driven activity in 289P is weak and looks to be nearly end, while there remains a chance of its longevity, provided that its steady state is retained. Overall, comet 289P is unlikely to be a reservoir for CO₂ and CO, but rather for water-ice.

5. DISCUSSION

5.1. *The Phoenicid Stream Mass*

We discuss three types of mass supply to form the Phoenicid meteoroid stream: steady, destructive and outburst. The sources considered are from comet 289P and/or its proposed precursor body.

5.1.1. *Steady Mass Supply*

The estimated mass-loss rates in dust (dust production rates) from observations of 289P can be compared with the mass of the Phoenicid stream. Jenniskens & Lyytinen (2005) estimated the stream mass $\sim 10^{11}$ kg from the 1956 Phoenicids, claiming that this could be consistent with the mass-loss activity (brightness) of an unconfirmed, few-km-scale precursor comet during a single orbital passage. The actual mass-loss rates are 0.01–0.02 kg s⁻¹ (Section 4.1), two to four orders of magnitude smaller than those of active JFCs (e.g. Gillan et al. 2024). This discrepancy suggests an alternative approach to estimating the Phoenicid stream mass: using the parent body mass, M_n , as a starting point. The other meteoroid streams show an approximate order unity agreement between the stream mass and the parent body mass. For example, the Taurid stream associated with comet 2P/Encke is estimated to have a mass of $\sim 10^{14}$ kg. Similar mass relationships are found in the α -Capricornid stream (from comet 169P/NEAT) and the Quadrantid stream (from 2003 EH₁), with estimated masses of $\sim 10^{13}$ kg each (Kasuga & Jewitt 2019). Given this consistency, we propose using the nucleus mass of 289P for the Phoenicid stream mass. The estimated nucleus mass of 289P is $M_n \sim 2 \times 10^{10}$ kg (with factors of several uncertainty) (Jewitt 2006), which is approximately one-fifth of the calculated stream mass $\sim 10^{11}$ kg (Jenniskens & Lyytinen 2005). By scaling M_n up and down by a factor of five, we estimate the possible range for the Phoenicid stream mass: $4 \times 10^9 \lesssim M_s \lesssim 10^{11}$ kg.

The Phoenicid stream is estimated to have been formed within $\tau_s \sim 300$ yrs (Watanabe et al. 2005). Assuming the observed mass-loss rate of 0.02 kg s⁻¹, the total stream mass would be only $\sim 1.9 \times 10^8$ kg, about an order of magnitude smaller than the possible stream mass range ($10^9 \sim 10^{11}$ kg). Therefore, we conclude that the Phoenicid stream was not solely produced through steady mass-loss at the observed rates.

Next, we focus on the size of the dust particles (meteoroids) and their distribution in the Phoenicid stream. In general, cometary streams mostly consist of near mm~cm-sized meteoroids (compact aggregates), as revealed by infrared space observations (2P, 73P, etc, Sykes & Walker 1992; Reach et al. 2000, 2007, 2009). Comparable size ranges, from nearly mm up to 10 cm, have been measured from the observations of meteor showers, such as the Taurids from 2P (Egal et al. 2022a) and the 2022 τ -Herculids (young stream, ~ 30 yrs old) from 73P (Koten et al. 2023). These larger particles, potentially containing much more mass, play a major role in determining the total stream mass. These observations imply that the Phoenicid stream is likely composed of meteoroids with a similar size distribution, ranging from nearly mm to 10 cm. We assume a distribution of dust particle radii follows a differential power law index γ , such that number of particles having radius between a and $a+da$ is written as $n(a)da = \Gamma a^{-\gamma}da$, with a constant Γ . The integrated mass of the particles, M , between

radii a_1 and a_2 over the last centuries is expressed as,

$$M = \frac{4}{3} N_{\text{orb}} \rho_d C_d \bar{a}, \quad (13)$$

where N_{orb} is number of perihelion passages of 289P, C_d is the cross-section of all the dust particles. The \bar{a} is the area-weighted mean particle radius, calculated by (Jewitt et al. 2023),

$$\bar{a} = \frac{\int_{a_1}^{a_2} a^{3-\gamma} da}{\int_{a_1}^{a_2} a^{2-\gamma} da}, \quad (14)$$

where a_1 is the minimum particle radius, a_2 is the maximum particle radius, and Γ is eliminated. We set $N_{\text{orb}} \sim 57$ ($\tau_s/P_{\text{orb}} = 300 \text{ yrs} / 5.3 \text{ yrs}$), $C_d = 1.5 \text{ km}^2$ (Visit *A* in Table 5), and $a_1 = 1 \mu\text{m}$ (*W1*-like), and $a_2 = 10 \text{ cm}$ (fireball-class meteoroids and the SSA model in Figure 5). With these values, we plot Equation (13) as a function of γ in the range $2.5 \leq \gamma \leq 4.5$, as shown in Figure 12. As the power law index (γ) decreases, the stream mass increases and approaches to the possible mass range due to the shift in the particle size distribution towards larger particles. A relevant comparison can be made with the size distribution of the observed meteoroid streams. The index range, $3.3 \leq \gamma \leq 4.4$, is estimated from the 1956 Phoenicids ($\gamma = 4$ from Venter 1957; Moorhead et al. 2024) and the other meteor showers associated with cometary sources (Blaauw et al. 2011; Egal et al. 2022a,b; Koten et al. 2023). We apply these results to estimate a plausible Phoenicid stream mass $M \sim 1.6 \times 10^8 \text{ kg}$ at $\gamma = 3.3$, still an order of magnitude lower than the possible range (Figure 12). The difference in mass ($\sim 3.84 \times 10^9 \text{ kg}$) corresponds to a spherical fragment having a radius $\sim 100 \text{ m}$ with an assumed density of 1000 kg m^{-3} ($= \rho_n$), equivalent to a 10 m-thick surface shell on the 160 m-radius nucleus of 289P. The leading conclusion is again that steady mass-loss near perihelion, even considering larger meteoroids and the distribution, cannot produce the Phoenicid stream.

5.1.2. Destructive Mass Supply

The Phoenicid meteoroid stream is likely replenished by the breakup of the 289P precursor body, but the exact cause remains unknown. Tidal forces from Jupiter at aphelion were unlikely due to their large distance (0.07~0.26 au) during their 1626–1819 interaction (Jenniskens & Lyttinen 2005). Other mechanisms must have led to the breakup. Here, we focus on the small size of the precursor body with the presumable radius $r_p \sim 170 \text{ m}$ (Section 5.1.1). Sub-kilometer active nuclei are expected to rapidly disintegrate due to rotational instability induced by outgassing torques, on timescales comparable to their orbital periods (Samarasinha & Mueller 2013; Jewitt 2021). We examine this possibility and its past active state. Outgassing may have spun-up the precursor nucleus, leading to its destruction on a timescale (Jewitt 1997, 2021),

$$\tau_{\text{dest}} = \left(\frac{16\pi^2}{15} \right) \left(\frac{\rho_n r_p^4}{k_T v_g P'_{\text{rot}}} \right) \left(\frac{1}{\overline{F_s} \pi r_{\text{ps}}^2} \right). \quad (15)$$

In this equation, k_T is the dimensionless effective moment arm of the outgassing¹⁶, P'_{rot} is the rotational period of the precursor body, $\overline{F_s}$ is the average sublimation mass-loss rate of water ice per unit

¹⁶ Quantity $k_T = 1$ corresponds to tangential emission, while $k_T = 0$ represents perfectly central outgassing (Jewitt 1997).

area around its orbit, r_{ps} is the radius of the ice sublimating area (patch) on the precursor body, and the other parameters are as described above. The spin-up timescale range is set between the orbital period $P_{\text{orb}} = 5.3$ yr (Table 2) and the empirically estimated timescale ~ 4 yr, given by $\sim 100 r_{\text{p(km)}}^2$ yr ($r_{\text{p(km)}} \sim 0.2$ expressed in km), for short-period comets (Jewitt 2021). Rotational destruction occurs within this range ($\sim 4 - 5.3$ yr), primarily determined by r_{ps} . Values of k_{T} derived from both models and observations are within the range $2 \times 10^{-4} \lesssim k_{\text{T}} \lesssim 5 \times 10^{-2}$ (Jewitt 1997; Belton et al. 2011; Drahus et al. 2011; Jewitt 2021). Small nuclei with low f_{A} , like 289P, are considered remnants (mostly unobserved) of destructive events caused by their large k_{T} (Jewitt 2021). Localized sublimation, as modeled for 289P (Section 3.2), also implies a larger k_{T} . We selected two representative values: $k_{\text{T}} = 0.05$ (Jewitt 1997) and the median value of $k_{\text{T}} = 0.007$ based on the short-period active comet measurements (Jewitt 2021). The larger value, $k_{\text{T}} = 0.05$, was prioritized. We computed the orbitally averaged subsolar sublimation \overline{F}_{s} for the precursor body with $a = 3.05$ au and $e = 0.69$ (Table 2), finding $\overline{F}_{\text{s}} = 4 \times 10^{-5} \text{ kg m}^{-2} \text{ s}^{-1}$ (Equation (A4), Jewitt 2021). To first order, we adopted $v_{\text{g}} \sim 480 \text{ m s}^{-1}$ near $R_{\text{h}} = 1$ au (Section 3.2) evidenced by the weak distance-dependence of $v_{\text{g}} \propto R_{\text{h}}^{-1/4}$ (Biver et al. 2002; Jewitt 2021). Assuming $P'_{\text{rot}} = P_{\text{rot}} \sim 8.8536$ hr (Section 3.3) and using the above parameters, we plot Equation (15) as a function of r_{ps} in Figure 13. Rotational destruction would have occurred for $k_{\text{T}} = 0.05$ when $22 \text{ m} \lesssim r_{\text{ps}} \lesssim 25 \text{ m}$ and for $k_{\text{T}} = 0.007$ when $59 \text{ m} \lesssim r_{\text{ps}} \lesssim 68 \text{ m}$, respectively. By comparison, setting perihelion distance $q = 0.96$ au finds the mass-loss rates $\sim 0.8 - 1.0 \text{ kg s}^{-1}$ ($k_{\text{T}} = 0.05$) or $\sim 6 - 8 \text{ kg s}^{-1}$ ($k_{\text{T}} = 0.007$), respectively. The corresponding fractional active area is $\sim (4 - 5) \times 10^{-3}$ ($k_{\text{T}} = 0.05$) and $\sim (3 - 4) \times 10^{-2}$ ($k_{\text{T}} = 0.007$), respectively. Both results are more than an order of magnitude larger than those of 289P, while comparable to typical JFCs. For the $k_{\text{T}} = 0.05$ case, the radius of sublimation area is at least $10 \times$ larger than $r_{\text{s}} \approx 2$ m on the 289P nucleus (Section 3.2), but the low mass-loss rates are remarkable. The precursor body, despite low activity, could have spun-up and disintegrated rapidly.

The destruction would have contributed to the Phoenicid stream mass. The exact timing of the precursor's rapid spin-up and subsequent destruction remains unknown, but we might be able to narrow it down to specific years. The 289P's orbit has been changed due to strong interactions with the Earth at perihelion and Jupiter at aphelion over short timescales (Jewitt 2006). The dynamical modeling proves that dust trails ejected before 1743 are too sparse to explain the 1956 Phoenicids, while those ejected in 1760–1808 are the major sources (Watanabe et al. 2005). In 1819, the comet was already very faint (Kronk 2003), suggesting that the precursor body had been disintegrated before that year. Given these constraints, the destructive event occurred probably in 1743–1819.

To verify it, we examine the potential contribution from the precursor's sublimation-driven mass-loss during the given timeframe. Using $\overline{F}_{\text{s}} = 4 \times 10^{-5} \text{ kg m}^{-2} \text{ s}^{-1}$ and the largest $r_{\text{ps}} \sim 25$ and 68 m (when $k_{\text{T}} = 0.05$ and 0.007 , respectively), the maximum delivered mass over 76 years ($= 1819 - 1743$) would be $(0.2 - 1) \times 10^9 \text{ kg}$. This accounts for only 25% or less of the minimum possible stream mass of $4 \times 10^9 \text{ kg}$ ($\lesssim M_{\text{s}}$). The $k_{\text{T}} = 0.05$ case would supply more than an order of magnitude smaller mass. These estimates can be consistent with the lack of observations before 1819 (Kronk 2003), most likely owing to its faintness due to low activity. Our findings strongly suggest that sublimation-driven activity from the precursor was insufficient to account for the Phoenicid stream mass. Thus, destructive mass supply was essential for its formation.

The Phoenicid meteoroid stream would comprise dust particles produced from both sublimation and disintegration processes. Each process ejects particles with speeds, $\gtrsim 0.5 \text{ m s}^{-1}$ from sublima-

tion (Watanabe et al. 2005) and $\sim 0.2 \text{ ms}^{-1}$ (\approx escape velocity) from disintegration, differing by a factor of few at least. Both particle types may have undergone similar dynamical evolution but may not have reached the Earth’s orbit simultaneously, depending on the timing of the destructive event. Jenniskens & Lyytinen (2005) estimated the stream mass ($\sim 10^{11} \text{ kg}$) based on the 1819 trail and particle sizes $\sim 1 \text{ mm}$. However, during the 1956 event, the 1819 trail was more than twice farther away from the Earth orbit ($\delta d_E = 1.4 \times 10^{-3} \text{ au}$) compared to the 1760–1808 trails ($\delta d_E = 6.3 \pm 0.8 \times 10^{-4} \text{ au}$), suggesting its limited contribution possibly only to the shower’s sub-peak (Table 1 and Figure 1, Watanabe et al. 2005). To estimate the stream mass, they assumed a broader dust trail along the Earth’s path, which is the cross-sectional area about $5 \times$ larger than that predicted from the distance to the 1760–1808 trails (δd_E), and integrated it along the comet’s orbit. This approach would have potentially encompassed both types of particles, regardless of their minor orbital differences.

5.1.3. Outburst Mass Supply

In 2013, 289P showed the distant activity with its coma and a tail at $R_h = 3.88 \text{ au}$ (Williams et al. 2013), which produced the mass of $M_d' = 3.1 \times 10^5 \text{ kg}$ (Appendix B). The event was likely an unexpected outburst of mass production, corresponding to $< 10^{-4}$ of the total stream mass. This is still too small to significantly contribute to the total stream mass, although there might be unseen similar events more.

All considerations here, the formation of the Phoenicid stream is likely a result of multiple mass-loss processes from comet 289P, including steady-state mass-loss near perihelion, unexpected outbursts, and, most importantly, the disintegration of the precursor body.

5.2. Nongravitational Acceleration

Nongravitational acceleration (NGA) on comets can serve as an indicator for estimating outgassing levels (mass-loss in gas). The NGA is decomposed into three types of independent parameters, A_1 in radial direction, A_2 in transverse (tangential component of the Yarkovsky force, influencing the object’s movement along its orbital path based on its rotation), A_3 in perpendicular to the plane of the orbit (Marsden et al. 1973). These parameters are calculated only when necessary to reconcile discrepancies between gravitational models and astrometric data, otherwise set to zero (Jewitt 2022). The radial component (A_1) is generally the largest due to the concentration of cometary outgassing on the heated, sunlit side of the nucleus. The resulting recoil force, primarily driven by the sublimation of water ice, acts directly away from the Sun.

In 2019 October–November, 289P was returning to its perihelion ($R_h = 1.45 \rightarrow 1.05 \text{ au}$), and the NGA parameters were obtained as $A_1 = -9.0 \times 10^{-10} \text{ au day}^{-2}$ and $A_2 = -8.2 \times 10^{-11} \text{ au day}^{-2}$.¹⁷ The negative A_1 -value suggests inward acceleration towards the Sun during its inbound, likely caused by a change in angular velocity driven by outgassing increase (Yeomans et al. 2004; Jewitt 2021). The absolute value is large enough to strongly support its cometary outgassing activity. If 289P were in the absence of sublimation of water ice, resembling a bare asteroid, the radial component should be $A_1 = 1.0 \times 10^{-12} \text{ au day}^{-2}$ at $R_h = 1.05 \text{ au}$ (Equation (2) of Hui & Jewitt 2022). This is three orders of magnitude smaller than the determined value from the astrometry. Therefore, 289P undoubtedly undergoes outgassing, consistent with the presence of sublimating ice.

¹⁷ MPEC 2019-W179. <https://www.minorplanetcenter.net/mpec/K19/K19WH9.html>.

The nongravitational acceleration, α_{NG} , is given as a function of sublimation rate of water ice, g (R_{h}), and expressed by (Marsden et al. 1973)

$$\alpha_{\text{NG}} = g(R_{\text{h}})(A_1^2 + A_2^2 + A_3^2)^{\frac{1}{2}}. \quad (16)$$

The function $g(R_{\text{h}})$ is defined by

$$g(R_{\text{h}}) = \alpha_{\text{M}} \left(\frac{R_{\text{h}}}{R_0} \right)^{-m} \left[1 + \left(\frac{R_{\text{h}}}{R_0} \right)^n \right]^{-k}, \quad (17)$$

where $R_0 = 2.808$ au, $m = 2.15$, $n = 5.093$, $k = 4.6142$, and $\alpha_{\text{M}} = 0.1113$ are constants determined from a fit to a model of sublimation of water ice. Substituting $R_{\text{h}}=1.01$ au (Visit *B*), $A_1 = -9.0 \times 10^{-10}$ au day⁻², $A_2 = -8.2 \times 10^{-11}$ au day⁻², and $A_3 = 0$ au day⁻² into Equations (16) and (17), we find $\alpha_{\text{NG}} = 1.8 \times 10^{-8}$ m s⁻² on 289P, about 0.0003 % of the solar gravitational acceleration (g_{\odot}). The result from 289P can be compared with those of well-characterized short-period comets. We focus on the perihelia, where the strongest outgassing produces the maximum nongravitational acceleration. The nucleus radii and the determined parameters A_1 , A_2 and A_3 are taken from the NASA/JPL Small-Body Database Lookup.¹⁸ The α_{NG} is normalized by the solar gravitational acceleration at each comet's perihelion distance (i.e. perihelion-normalized NGA), as given by (Jewitt et al. 2021),

$$\alpha'_{\text{NG}} = \frac{g(q)q^2}{GM_{\odot}}(A_1^2 + A_2^2 + A_3^2)^{\frac{1}{2}}, \quad (18)$$

where G is the gravitational constant, M_{\odot} is the Solar mass, and q is the perihelion distance in meters. Substituting $q = 0.96$ au into Equation (17), we obtain $g(q) = 1.097$. Using Equation (18) with the parameters above, we find $\alpha'_{\text{NG}} = 3.1 \times 10^{-6}$. Likewise we derive α'_{NG} for known comets: two Halley-type (1P and 55P), three Encke-type (2P, 87P, and 147P), and nineteen JFCs (4P, 6P, 7P, 8P, 9P, 10P, 19P, 21P, 22P, 24P, 26P, 43P, 65P, 67P, 76P, 81P, 96P, 103P, and 106P). Figure 14 shows the resulting relationship between nucleus radius and α'_{NG} . We find Halley-type of $\alpha'_{\text{NG}} = 3.6 \pm 2.4 \times 10^{-6}$, Encke-type of $\alpha'_{\text{NG}} = 2.2 \pm 2.4 \times 10^{-5}$, and JFCs (except 289P) of $\alpha'_{\text{NG}} = 4.3 \pm 4.3 \times 10^{-6}$, respectively. The median of known comets is $\alpha'_{\text{NG}} = 2.7 \times 10^{-6}$. The 289P ($\alpha'_{\text{NG}} = 3.1 \times 10^{-6}$) falls within the range $10^{-7} \lesssim \alpha'_{\text{NG}} \lesssim 10^{-5}$, where most km-sized comets demonstrate (Jewitt et al. 2021). In contrast, 289P shows a moderately lower value among the other small-sized nuclei with radii of 100(s) meters. To investigate the relationship between radius and α'_{NG} , we conducted a least-squares fit of a power law to the data for known comets (yellow symbols). The resulting dashed line suggests a trend of increasing α'_{NG} with decreasing radius. It is reasonable to expect that smaller nuclei would experience significantly greater acceleration if the outgassing levels were comparable across all sizes. While this trend is evident, 289P shows about an order of magnitude smaller α'_{NG} than the fitted line. This suggests that 289P's outgassing level is rather lower than those of known comets with comparable size. Note that this assessment is based on the limited samples of sub-km nuclei (several of them). To establish a more statistically robust comparison, deriving α'_{NG} from a larger sample of sub-km nuclei, such as those from the upcoming LSST survey, would provide valuable insights. While this current estimate of the α'_{NG} -trend might be approximate and influenced by selection bias, it can still serve as a useful benchmark for assessing outgassing levels across various comet populations.

¹⁸ <https://ssd.jpl.nasa.gov/tools/>

6. SUMMARY

We present NEOWISE observations for comet 289P/Blanpain near perihelion taken on two opportunities: UT 2019-10-30 ($R_h = 1.20$ au, inbound) and UT 2020-01-11/12 ($R_h = 1.01$ au, outbound). The near-infrared data, $3.4\mu\text{m}$ ($W1$) and $4.6\mu\text{m}$ ($W2$), are used to analyze its faint activity driven by sublimation of water ice and resulting product, the Phoenicid meteoroid stream. Based on the 1956 Phoenicids, considering both meteor observations and trail theory, we set proper constraints for dust production from the limited sublimating ice patch area. The following are findings.

1. The ejected dust mass is $M_d = 4100 \pm 200$ kg (inbound) and 1700 ± 200 kg (outbound), respectively.
2. The dust production rates are $Q_{\text{dust}} = 0.01 - 0.02 \text{ kg s}^{-1}$ while 289P orbits from heliocentric distance $R_h = 1.20$ to 1.01 au around perihelion, indicating weak activity as previously observed.
3. The dust-to-gas production ratio ranges $2 \leq f_{\text{dg}} \leq 6$.
4. The fractional active area $f_A = 3.8 \pm 1.9 \times 10^{-5}$ is the smallest in the active Jupiter family comets yet reported.
5. The absence of $4.6\mu\text{m}$ ($W2$) excess suggests that 289P contains negligible amount of CO_2 and CO .
6. The light curve, derived from the weighted mean of $W1$ and $W2$ magnitudes, shows a distinct peak amplitude with a possible rotation period $P_{\text{rot}} = 8.8536 \pm 0.3860$ hr, but definitive conclusion is pending due to the low significance level of $\sim 30\%$.
7. The perihelion-normalized nongravitational acceleration, $\alpha'_{\text{NG}} = 3.1 \times 10^{-6}$, is approximately an order of magnitude smaller than the trend observed in well-studied comets, consistent with the weak outgassing.
8. Current dust production from 289P, despite a plausible set of particle size and distribution, is an order of magnitude too small to account for the probable mass of the Phoenicid stream within ~ 300 year dynamical lifetime. 289P is most likely a remnant comet of a sub-km precursor body that may have been a low active JFC. Outgassing quickly induced rotational destruction, led to additional mass supply probably in 1743–1819.

TK is grateful to Junji Nakamura for observing the 1956 Phoenicid meteor shower and sharing his firsthand story. The author thanks Jun-ichi Watanabe, Mikiya Sato, Chie Tsuchiya, David Jewitt, Joseph R. Masiero, Man-To Hui, Dave G. Milewski, and Budi Dermawan, for support. This publication makes use of data products from the *Wide-field Infrared Survey Explorer*, which is a joint project of the University of California, Los Angeles, and the Jet Propulsion Laboratory/California Institute of Technology, funded by the National Aeronautics and Space Administration. Also, this publication makes use of data products from the Near-Earth Object Wide-field Infrared Survey Explorer (NEOWISE), which is a joint project of the Jet Propulsion Laboratory/California Institute of Technology and the University of Arizona. NEOWISE is funded by the National Aeronautics and Space Administration. This publication uses data obtained from the NASA Planetary Data System (PDS). This research has made use of data and services provided by the International Astronomical Union’s Minor Planet Center. This research has made use of the NASA/IPAC Infrared Science Archive, which is funded by the National Aeronautics and Space Administration and operated by the California Institute of Technology, under contract with the National Aeronautics and Space Administration. We would like to address special thanks to anonymous reviewers and to Maria Womack for scientific editor.

Facilities: NEOWISE, WISE

APPENDIX

A. THERMAL DIFFUSIVITY

We inferred the thermal diffusivity of 289P, κ ($\text{m}^2 \text{s}^{-1}$), from thermal inertia measurements of JFC 67P by Rosetta’s VIRTIS (Visible InfraRed and Thermal Imaging Spectrometer). The observed values ranged between 40 and 160 $\text{J K}^{-1} \text{m}^{-2} \text{s}^{-1/2}$ (Marshall et al. 2018), with lower values ($< 50 \text{ J K}^{-1} \text{m}^{-2} \text{s}^{-1/2}$) being more common (Tosi et al. 2019). These findings are indicative of a highly porous structure with low thermal diffusivity (Keller & Kührt 2020). Thermal inertia, I ($\text{J K}^{-1} \text{m}^{-2} \text{s}^{-1/2}$), is defined as

$$I = \sqrt{k\rho_b c_p}, \quad (\text{A1})$$

where k is the thermal conductivity, $\rho_b = 538 \text{ kg m}^{-3}$ is the bulk density of the 67P nucleus (Pätzold et al. 2019), $c_p = 1000 \text{ J kg}^{-1} \text{K}^{-1}$ is the assumed heat capacity of the pebbles (Blum et al. 2017; Fulle et al. 2020). With $I = 40\text{--}160 \text{ J K}^{-1} \text{m}^{-2} \text{s}^{-1/2}$, we find $k = 3 \times 10^{-3} \text{--} 5 \times 10^{-2} \text{ W m}^{-1} \text{K}^{-1}$. Thermal diffusivity is calculated by $\kappa = k/(\rho_b c_p)$. Substituting the above parameters, we obtain $\kappa \sim 10^{-8}\text{--}10^{-7} \text{ m}^2 \text{s}^{-1}$. The conduction timescale for 289P is given by $\tau_c \sim r_n^2/\kappa$, where $r_n \sim 160 \text{ m}$. Substitution κ derives $\tau_c \sim 8 \times 10^{3-4} \text{ yr}$.

B. 2013 ACTIVITY IN COMET 289P/BLANPAIN AT $R_H = 3.88 \text{ AU}$

On 2013 July 5 and 6 (UT), observations by the Pan-STARRS and other telescopes confirmed the presence of a coma and tail for comet 289P/Blanpain at the heliocentric distance $R_h = 3.88 \text{ au}$, and the apparent visual magnitude was $m_V = 19.5 \sim 17.5 \text{ mag}$ (Williams et al. 2013). Here, we estimate the relevant ejected dust mass, M'_d , focusing on the contribution from coma (not tail). The apparent

visual magnitude, m_V , was corrected to the absolute magnitude, $m_V(1, 1, 0)$, using

$$m_V(1, 1, 0) = m_V - 5 \log(R_h \Delta) + 2.5 \log_{10}(\Phi_{\text{HM}}(\alpha)), \quad (\text{B2})$$

where R_h and Δ are the heliocentric and geocentric distances (both in au), and $\Phi_{\text{HM}}(\alpha)$ is the Halley-Marcus composite phase function for dust scattering in coma (Schleicher et al. 1998; Marcus 2007) in which α is the phase angle (in degrees). Substituting $R_h = 3.88$ au, $\Delta = 2.87$ au, $\alpha = 2^\circ.5$ (i.e., $\Phi_{\text{HM}}(2^\circ.5) = 0.90$) (on UT 2013 July 6, 13:00 from NASA/JPL HORIZONS) and maximum $m_V = 17.5$ mag into Equation (B2), we find the absolute magnitude $m_V(1, 1, 0) = 12.2$ mag. The effective scattering cross-section of dust and nucleus within the photometry aperture, C_e (km²), is given by (Russell 1916)

$$C_e = \frac{\pi \times 2.24 \times 10^{16}}{p_V} 10^{0.4(m_{V\odot} - m_V(1,1,0))}, \quad (\text{B3})$$

where $m_{V\odot} = -26.75$ mag is the apparent visual magnitude of the Sun (Drilling & Landolt 2000). With $p_V = 0.04$ (Section 3.4) and $m_V(1, 1, 0) = 12.2$ mag into Equation (B3), we find $C_e = 463$ km². By subtracting the nucleus cross-section (C_n) from the effective scattering cross-section (C_e), we obtain the cross-section of dust, $C_d = 462.9 \pm 0.1$ km². Using Equation (7) with $a_d = 0.5$ μm (visual wavelength), $\rho_d = 1000$ kg m⁻³ (assumed bulk density), and the obtained C_d , we find the ejected dust mass $M'_d \approx 3.1 \times 10^5$ kg.

The mechanism driving sudden activity near 4 au remains uncertain. Crystallization of amorphous ice is unlikely due to the 289P's internal temperature of ~ 180 K (Section 4.2), exceeding the critical temperature of ~ 140 K (Priyalnik & Jewitt 2022). Seasonal effects on the rotating nucleus could contribute to the distant activity, as previously unexposed subsurface ice-rich region in the dark hemisphere turned into sunlight. However, still unclear whether the resulting sublimation of water ice and venting of integrated internal gas pressure can fully explain the observed massive dust ejection. The Rosetta mission to 67P served as a precedent. Amorphous water ice is not yet confirmed within the nucleus (Keller & Kürt 2020). The outbursts from some ice patches (Filacchione et al. 2019) and continuous (background) activity, including morphological changes on the bi-lobe shape (e.g. mass-wasting, cliff collapse, pit formation) caused by diurnal and seasonal effects (El-Maarry et al. 2019), have been observed. The understanding of these physical processes remains limited (Keller & Kürt 2020). Future missions, such as a spacecraft sample-return from 289P in the 2030s (Wakita et al. 2023) and a flyby observation by Comet Interceptor (backup plan in 2035) (Schwamb et al. 2020; Jones et al. 2024), would provide more understanding of the nature.

REFERENCES

- Agarwal, J., Kim, Y., Kelley, M. S. P., & Marschall, R. 2023, arXiv e-prints, arXiv:2309.12759
- A'Hearn, M. F., Schleicher, D. G., Millis, R. L., Feldman, P. D., & Thompson, D. T. 1984, AJ, 89, 579
- Asher, D. J. 2000, in Proceedings of the International Meteor Conference, 18th IMC, Frasso Sabino, Italy, 1999, ed. R. Arlt, 5–21
- Bauer, J. M., Choi, Y.-J., Weissman, P. R., et al. 2008, PASP, 120, 393
- Bauer, J. M., Gicquel, A., Kramer, E., & Meech, K. J. 2021, PSJ, 2, 34
- Bauer, J. M., Walker, R. G., Mainzer, A. K., et al. 2011, ApJ, 738, 171
- Bauer, J. M., Kramer, E., Mainzer, A. K., et al. 2012, ApJ, 758, 18

- Bauer, J. M., Stevenson, R., Kramer, E., et al. 2015, *ApJ*, 814, 85
- Belton, M. J. S., Meech, K. J., Chesley, S., et al. 2011, *Icarus*, 213, 345
- Biver, N., Bockelée-Morvan, D., Colom, P., et al. 2002, *Earth Moon and Planets*, 90, 5
- Blaauw, R. C., Campbell-Brown, M. D., & Weryk, R. J. 2011, *MNRAS*, 414, 3322
- Blaauw, R. C., Suggs, R. M., & Cooke, W. J. 2014, *M&PS*, 49, 45
- Blum, J., Gundlach, B., Krause, M., et al. 2017, *MNRAS*, 469, S755
- Bohren, C. F., & Huffman, D. R. 1983, *Absorption and scattering of light by small particles*
- Bouziani, N., & Jewitt, D. 2022, *ApJ*, 924, 37
- Buratti, B. J., Hicks, M. D., Soderblom, L. A., et al. 2004, *Icarus*, 167, 16
- Cremonese, G., Fulle, M., Cambianica, P., et al. 2020, *ApJL*, 893, L12
- Cutri, R. M., Wright, E. L., Conrow, T., et al. 2012, *Explanatory Supplement to the WISE All-Sky Data Release Products, Explanatory Supplement to the WISE All-Sky Data Release Products*, ,
- Cutri, R. M., Mainzer, A., Conrow, T., et al. 2015, *Explanatory Supplement to the NEOWISE Data Release Products, Explanatory Supplement to the NEOWISE Data Release Products*, ,
- Drahus, M., Jewitt, D., Guilbert-Lepoutre, A., et al. 2011, *ApJL*, 734, L4
- Drilling, J. S., & Landolt, A. U. 2000, in *Allen's Astrophysical Quantities*, ed. A. N. Cox, 381
- Duncan, M., Levison, H., & Dones, L. 2004, in *Comets II*, ed. H. U. K. M. C. Festou & H. A. Weaver (University of Arizona Press, Tucson), 193–204
- Egal, A., Brown, P. G., Wiegert, P., & Kipreos, Y. 2022a, *MNRAS*, 512, 2318
- Egal, A., Wiegert, P., & Brown, P. G. 2022b, *MNRAS*, 515, 2800
- El-Maarry, M. R., Groussin, O., Keller, H. U., et al. 2019, *SSRv*, 215, 36
- Fernández, Y. R., Sheppard, S. S., & Jewitt, D. C. 2003, *AJ*, 126, 1563
- Fernández, Y. R., Kelley, M. S., Lamy, P. L., et al. 2013, *Icarus*, 226, 1138
- Filacchione, G., Groussin, O., Herny, C., et al. 2019, *SSRv*, 215, 19
- Foglia, S., Micheli, M., Ridley, H. B., Jenniskens, P., & Marsden, B. G. 2005, *IAU Circ.*, 8485
- Fulle, M. 2004, in *Comets II*, ed. M. C. Festou, H. U. Keller, & H. A. Weaver, 565
- Fulle, M., Blum, J., Rotundi, A., et al. 2020, *MNRAS*, 493, 4039
- Fulle, M., Marzari, F., Della Corte, V., et al. 2016, *ApJ*, 821, 19
- Gicquel, A., Bauer, J. M., Kramer, E. A., Mainzer, A. K., & Masiero, J. R. 2023, *PSJ*, 4, 3
- Gillan, A. F., Fitzsimmons, A., Denneau, L., et al. 2024, *PSJ*, 5, 25
- Gilliland, R. L., & Fisher, R. 1985, *PASP*, 97, 285
- Graykowski, A., & Jewitt, D. 2019, *AJ*, 158, 112
- Harmon, J. K., Nolan, M. C., Ostro, S. J., & Campbell, D. B. 2004, in *Comets II*, ed. M. C. Festou, H. U. Keller, & H. A. Weaver, 265
- Hovis, W. A., J., & Callahan, W. R. 1966, *Journal of the Optical Society of America (1917-1983)*, 56, 639
- Hsieh, H. H., & Haghhighipour, N. 2016, *Icarus*, 277, 19
- Hui, M.-T., & Jewitt, D. 2022, *AJ*, 164, 236
- Huruhata, M., & Nakamura, J. 1957, *Tokyo Astronomical Bulletin*, 2nd Ser., 99, 1053
- Jenniskens, P. 2006, *Meteor Showers and their Parent Comets*
- Jenniskens, P., & Lyytinen, E. 2005, *AJ*, 130, 1286
- Jewitt, D. 1991, in *Astrophysics and Space Science Library*, Vol. 167, *IAU Colloq. 116: Comets in the post-Halley era*, ed. J. Newburn, R. L., M. Neugebauer, & J. Rahe, 19
- Jewitt, D. 1997, *Earth Moon and Planets*, 79, 35
- . 2006, *AJ*, 131, 2327
- . 2021, *AJ*, 161, 261
- . 2022, *AJ*, 164, 158
- Jewitt, D., Asmus, D., Yang, B., & Li, J. 2019, *AJ*, 157, 193
- Jewitt, D., & Hsieh, H. 2006, *AJ*, 132, 1624
- Jewitt, D., Hsieh, H., & Agarwal, J. 2015, in *Asteroids IV*, ed. P. Michel, F. E. DeMeo, & W. F. Bottke (University of Arizona Press), 221–241
- Jewitt, D., & Hsieh, H. H. 2022, *arXiv e-prints*, arXiv:2203.01397
- Jewitt, D., Ishiguro, M., Weaver, H., et al. 2014, *AJ*, 147, 117
- Jewitt, D., Kim, Y., Mattiazzo, M., et al. 2023, *AJ*, 165, 122

- Jewitt, D., Kim, Y., Mutchler, M., et al. 2021, *AJ*, 161, 188
- . 2020, *ApJL*, 896, L39
- Jewitt, D., & Li, J. 2010, *AJ*, 140, 1519
- Jewitt, D. C. 2004, in *Comets II*, ed. M. C. Festou, H. U. Keller, & H. A. Weaver, 659
- Jewitt, D. C., & Meech, K. J. 1987, *ApJ*, 317, 992
- Jones, G. H., Snodgrass, C., Tubiana, C., et al. 2024, *SSRv*, 220, 9
- Jopek, T. J., & Jenniskens, P. M. 2011, in *Meteoroids: The Smallest Solar System Bodies*, ed. M. D. E. H. B. F. Cooke, W. J. & D. Janches (Colorado, USA: Proceedings of the Meteoroids Conference held in Breckenridge, NASA/CP-2011-216469), 7–13
- Kasuga, T., Balam, D. D., & Wiegert, P. A. 2010, *AJ*, 140, 1806
- Kasuga, T., & Jewitt, D. 2015, *AJ*, 150, 152
- . 2019, in *Meteoroids: Sources of Meteors on Earth and Beyond*, Ryabova G. O., Asher D. J., and Campbell-Brown M. D. (eds.), Cambridge, UK: Cambridge University Press, 336 pp., ISBN 9781108426718, 2019, p. 187-209, 187
- Kasuga, T., & Masiero, J. R. 2022, *AJ*, 164, 193
- Keller, H. U., & Kühr, E. 2020, *SSRv*, 216, 14
- Knight, M. M., Kokotanekova, R., & Samarasinha, N. H. 2023, arXiv e-prints, arXiv:2304.09309
- Kokotanekova, R., Snodgrass, C., Lacerda, P., et al. 2017, *MNRAS*, 471, 2974
- Koten, P., Shrubbený, L., Spurný, P., et al. 2023, *A&A*, 675, A70
- Kronk, G. W. 2003, *Cometography: A Catalog of Comets, Volume 2: 1800-1899*
- . 2014, *Meteor Showers: An Annotated Catalog*, doi:10.1007/978-1-4614-7897-3
- Lamy, P. L., Toth, I., Fernandez, Y. R., & Weaver, H. A. 2004, in *Comets II*, ed. M. C. Festou, H. U. Keller, & H. A. Weaver (Tucson: University of Arizona Press), 223–264
- Lebofsky, L. A., Sykes, M. V., Tedesco, E. F., et al. 1986, *Icarus*, 68, 239
- Lindblad, B. A. 1987, in *The Evolution of the Small Bodies of the Solar System*, ed. M. Fulchignoni & L. Kresak, 229
- Lomb, N. R. 1976, *Ap&SS*, 39, 447
- Luu, J. X., & Jewitt, D. C. 1992, *Icarus*, 97, 276
- Mainzer, A., Grav, T., Masiero, J., et al. 2011, *ApJ*, 736, 100
- Mainzer, A., Bauer, J., Cutri, R. M., et al. 2014, *ApJ*, 792, 30
- Marcus, J. N. 2007, *International Comet Quarterly*, 29, 39
- Marschall, R., Zakharov, V., Tubiana, C., et al. 2022, *A&A*, 666, A151
- Marsden, B. G., Sekanina, Z., & Yeomans, D. K. 1973, *AJ*, 78, 211
- Marshall, D., Groussin, O., Vincent, J. B., et al. 2018, *A&A*, 616, A122
- Masci, F. 2013, *ICORE: Image Co-addition with Optional Resolution Enhancement, Astrophysics Source Code Library*, record ascl:1302.010, ,
- Micheli, M. 2005, *Astronomia. La rivista dell'Unione Astrofili Italiani*, 1, 47
- Milewski, D. G., Masiero, J. R., Pittichová, J., et al. 2024, *AJ*, 167, 99
- Moorhead, A. V., Cooke, W. J., Brown, P. G., & Campbell-Brown, M. D. 2024, arXiv e-prints, arXiv:2408.04612
- NEOWISE Team. 2020, *NEOWISE-R Single Exposure (L1b) Source Table*, IPAC, doi:10.26131/IRSA144. <https://catcopy.ipac.caltech.edu/doi/doi.php?id=10.26131>
- Ootsubo, T., Kawakita, H., Hamada, S., et al. 2012, *ApJ*, 752, 15
- Pätzold, M., Andert, T. P., Hahn, M., et al. 2019, *MNRAS*, 483, 2337
- Pittichová, J., Woodward, C. E., Kelley, M. S., & Reach, W. T. 2008, *AJ*, 136, 1127
- Prialnik, D., Benkhoff, J., & Podolak, M. 2004, *Modeling the structure and activity of comet nuclei*, ed. M. C. Festou, H. U. Keller, & H. A. Weaver, 359
- Prialnik, D., & Jewitt, D. 2022, arXiv e-prints, arXiv:2209.05907
- Reach, W. T., Kelley, M. S., & Sykes, M. V. 2007, *Icarus*, 191, 298
- Reach, W. T., Sykes, M. V., Lien, D., & Davies, J. K. 2000, *Icarus*, 148, 80
- Reach, W. T., Vaubaillon, J., Kelley, M. S., Lisse, C. M., & Sykes, M. V. 2009, *Icarus*, 203, 571
- Ridley, H. B. 1957, *Circulars of the British Astronomical Association*, 382
- Ridley, H. B. 1963, *Monthly Notes of the Astronomical Society of South Africa*, 22, 42
- Rosser, J. D., Bauer, J. M., Mainzer, A. K., et al. 2018, *AJ*, 155, 164
- Rotundi, A., Sierks, H., Della Corte, V., et al. 2015, *Science*, 347, aaa3905
- Russell, H. N. 1916, *Proceedings of the National Academy of Science*, 2, 74

- Samarasinha, N. H., & A'Hearn, M. F. 1991, *Icarus*, 93, 194
- Samarasinha, N. H., & Mueller, B. E. A. 2013, *ApJL*, 775, L10
- Samarasinha, N. H., Mueller, B. E. A., Belton, M. J. S., & Jorda, L. 2004, in *Comets II*, ed. M. C. Festou, H. U. Keller, & H. A. Weaver, 281
- Sato, M. 2003, *WGN, Journal of the International Meteor Organization*, 31, 59
- Scargle, J. D. 1982, *ApJ*, 263, 835
- Schleicher, D. G., Millis, R. L., & Birch, P. V. 1998, *Icarus*, 132, 397
- Schwamb, M. E., Knight, M. M., Jones, G. H., et al. 2020, *Research Notes of the American Astronomical Society*, 4, 21
- Stevenson, R., Bauer, J. M., Cutri, R. M., Mainzer, A. K., & Masci, F. J. 2015, *ApJL*, 798, L31
- Sykes, M. V., & Walker, R. G. 1992, *Icarus*, 95, 180
- Tancredi, G. 2014, *Icarus*, 234, 66
- Tancredi, G., Fernández, J. A., Rickman, H., & Licandro, J. 2006, *Icarus*, 182, 527
- Ticha, J., Tichy, M., Kocer, M., et al. 2003, *Minor Planet Electronic Circulars*, 2003-W41
- Tosi, F., Capaccioni, F., Capria, M. T., et al. 2019, *Nature Astronomy*, 3, 649
- Venter, S. C. 1957, *Monthly Notes of the Astronomical Society of South Africa*, 16, 6
- Wakita, S., Kurokawa, H., Shimaki, Y., et al. 2023, in *LPI Contributions*, Vol. 2851, *Asteroids, Comets, Meteors Conference*, 2029
- Watanabe, J.-I., Sato, M., & Kasuga, T. 2005, *PASJ*, 57, L45
- Whipple, F. L. 1951, *ApJ*, 113, 464
- Williams, G. V., Sato, H., Marsden, B. G., & Nakano, S. 2013, *Central Bureau Electronic Telegrams*, 3574, 1
- WISE Team. 2020a, *WISE All-Sky Single Exposure (L1b) Source Table*, IPAC, doi:10.26131/IRSA139.
<https://catcopy.ipac.caltech.edu/doi/doi.php?id=10.26131>
- . 2020b, *WISE 3-Band Cryo Single Exposure (L1b) Source Table*, IPAC, doi:10.26131/IRSA127.
<https://catcopy.ipac.caltech.edu/doi/doi.php?id=10.26131>
- . 2020c, *NEOWISE 2-Band Post-Cryo Single Exposure (L1b) Source Table*, IPAC, doi:10.26131/IRSA124.
<https://catcopy.ipac.caltech.edu/doi/doi.php?id=10.26131>
- Womack, M., Sarid, G., & Wierzchos, K. 2017, *PASP*, 129, 031001
- Wright, E. L., Eisenhardt, P. R. M., Mainzer, A. K., et al. 2010, *AJ*, 140, 1868
- Yamamoto, T. 1985, *A&A*, 142, 31
- Yeomans, D. K., Chodas, P. W., Sitarski, G., Szutowicz, S., & Królikowska, M. 2004, in *Comets II*, ed. M. C. Festou, H. U. Keller, & H. A. Weaver, 137
- Yue, Y., Liu, J., & Wang, X. 2023, *Journal of Geophysical Research (Planets)*, 128, e2022JE007329

Table 1. NEOWISE Observation Log

Visit	MJD ^a	UT Date	RA ^b	DEC ^c	R_h ^d	Δ ^e	α ^f	$W1$ ^g	$W2$ ^h
			(deg)	(deg)	(au)	(au)	(deg)	(mag)	(mag)
A	58786.0688	2019-10-30 01:39:05.796	336.618	-24.534	1.2056	0.4018	49.5624	15.181±0.563	<i>i</i>
	58786.1997	2019-10-30 04:47:35.840	336.594	-24.521	1.2046	0.4014	49.6867	<i>j</i>	<i>j</i>
	58786.2650	2019-10-30 06:21:39.862	336.582	-24.514	1.2041	0.4012	49.7487	<i>i</i>	13.033±0.151
	58786.3304	2019-10-30 07:55:54.884	336.570	-24.508	1.2035	0.4010	49.8108	15.800±0.392	13.490±0.198
	58786.3959	2019-10-30 09:30:09.910	336.558	-24.501	1.2030	0.4008	49.8730	15.037±0.367	<i>j</i>
	58786.4613	2019-10-30 11:04:24.932	336.547	-24.494	1.2025	0.4006	49.9351	14.916±0.307	12.231±0.077
	58786.5267	2019-10-30 12:38:28.954	336.535	-24.487	1.2020	0.4004	49.9970	<i>j</i>	13.376±0.202
	58786.6576	2019-10-30 15:46:59.002	336.512	-24.474	1.2009	0.3999	50.1212	15.565±0.259	13.032±0.133
	58786.7884	2019-10-30 18:55:18.046	336.489	-24.460	1.1999	0.3995	50.2452	<i>j</i>	12.656±0.121
B	58859.9303	2020-01-11 22:19:39.686	15.406	+57.207	1.0099	0.0910	70.5400	<i>k</i>	<i>k</i>
	58859.9957	2020-01-11 23:53:54.721	15.721	+57.442	1.0102	0.0910	70.3560	12.471±0.045	9.743±0.039
	58860.1266	2020-01-12 03:02:24.787	16.364	+57.910	1.0108	0.0910	69.9862	12.529±0.052	9.718±0.039

NOTE—Visit A (MJD 58786: UT 2019-10-30, inbound) and Visit B (MJD 58860: UT 2020-01-11/12, outbound) are defined.

^a Modified Julian Date of the mid-point of the observation.

^b Right ascension (J2000).

^c Declination (J2000).

^d Heliocentric distance.

^e *WISE*-centric distance.

^f Phase angle.

^g Measured magnitude at *W1* from the single-exposure frame.

^h Measured magnitude at *W2* from the single-exposure frame.

ⁱ SNR < 1.

^j The 289P image is unconfirmed or too weak to measure the FWHM.

^k Contaminated by a star.

Table 2. Orbital Property of Comet 289P/Blanpain (2003 WY₂₅)

${}_a a$	${}_e b$	${}_i c$	${}_q d$	${}_\omega e$	${}_\Omega f$	${}_Q g$	${}_{P_{\text{orb}}} h$	${}_{T_J} i$
(au)		(deg)	(au)	(deg)	(deg)	(au)	(yr)	
3.045	0.685	5.897	0.959	9.849	68.924	5.132	5.315	2.817

NOTE— From NASA JPL Small-Body Database Lookup (2458746.5 (2019-Sep-20.0): Solution Date 2024-Jul-26)

a Semimajor axis.

b Eccentricity.

c Inclination.

d Perihelion distance.

e Argument of perihelion.

f Longitude of ascending node.

g Aphelion distance.

h Orbital period.

i Tisserand parameter with respect to Jupiter. $T_J < 3.08$ for comets and $T_J > 3.08$ for asteroids, if $a < a_J = 5.2$ au (Jewitt et al. 2015). For reference, we list other comet-asteroid thresholds of $T_J = 3.05$ (Tancredi 2014) and $T_J = 3.10$ (Hsieh & Haghhighipour 2016) (see a review, Jewitt & Hsieh 2022).

Table 3. Magnitude and Flux Density

Visit	$W1^a$ (mag)	$W2^b$ (mag)	$W1^c$ (Jy)	$W2^d$ (Jy)
A^e	15.903 ± 0.133	13.035 ± 0.066	$1.35 \pm 0.17 \times 10^{-4}$	$1.05 \pm 0.06 \times 10^{-3}$
B^f	12.525 ± 0.046	9.714 ± 0.039	$3.02 \pm 0.13 \times 10^{-3}$	$2.24 \pm 0.08 \times 10^{-2}$

NOTE—Magnitudes are measured from the composite images and converted to flux densities for each band (Wright et al. 2010).

^a Measured magnitude at $W1$ from the composite image.

^b Measured magnitude at $W2$ from the composite image.

^c Flux density, converted from magnitude at $W1$.

^d Flux density, converted from magnitude at $W2$.

^e MJD 58786: UT 2019-10-30, inbound. $R_h=1.20$ au, $\Delta=0.40$ au, and $\alpha=49.8^\circ$.

^f MJD 58860: UT 2020-01-11/12, outbound. $R_h=1.01$ au, $\Delta=0.09$ au, and $\alpha=70.2^\circ$.

Table 4. Weighted Mean of $W1$ and $W2$ Magnitudes

Visit	MJD ^{<i>a</i>}	$W1$ ^{<i>b</i>} (mag)	$W2$ ^{<i>c</i>} (mag)	W_{wm} ^{<i>d</i>} (mag)
A	58786.0688	15.181±0.563 ^{<i>e</i>}	11.662 ^{<i>h</i>}	12.056±0.188
	58786.1997	15.491 ^{<i>f</i>}	12.577 ^{<i>h</i>}	13.474±0.166
	58786.2650	15.645 ^{<i>f</i>}	13.033±0.151 ^{<i>g</i>}	13.561±0.135
	58786.3304	15.800±0.392 ^{<i>e</i>}	13.490±0.198 ^{<i>g</i>}	13.960±0.177
	58786.3959	15.037±0.367 ^{<i>e</i>}	12.860 ^{<i>h</i>}	13.358±0.176
	58786.4613	14.916±0.307 ^{<i>e</i>}	12.231±0.077 ^{<i>g</i>}	12.390±0.075
	58786.5267	15.132 ^{<i>f</i>}	13.376±0.202 ^{<i>g</i>}	13.924±0.168
	58786.6576	15.565±0.259 ^{<i>e</i>}	13.032±0.133 ^{<i>g</i>}	13.561±0.118
	58786.7884	15.997 ^{<i>f</i>}	12.656±0.121 ^{<i>g</i>}	13.123±0.112

NOTE—For light curve analysis with W_{wm} from Visit A (MJD 58786: UT 2019-10-30, inbound).

^{*a*} Modified Julian Date of the mid-point of the observation.

^{*b*} Magnitude at $W1$ from the single-exposure frame.

^{*c*} Magnitude at $W2$ from the single-exposure frame.

^{*d*} Weighted mean of $W1$ and $W2$ magnitudes.

^{*e*} Measured magnitude at $W1$ from Table 1.

^{*f*} Interpolated/extrapolated magnitude at $W1$. Assumed uncertainty is 0.3 mag.

^{*g*} Measured magnitude at $W2$ from Table 1.

^{*h*} Interpolated/extrapolated magnitude at $W2$. Assumed uncertainty is 0.2 mag.

Table 5. Properties of Dust Production

Visit	D_e^a (km)	C_d^b (km ²)	M_d^c (kg)	Q_{dust}^d (kg s ⁻¹)	$Q_{Af\rho}^e$ (kg s ⁻¹)
A^f	1.43±0.04	1.53±0.09	4100±200	1.0±0.1×10 ⁻²	1.0±0.2×10 ⁻² h
B^g	0.96±0.01	0.64±0.08	1700±200	2.0±0.3×10 ⁻²	4.0±0.2×10 ⁻² i

NOTE—

^a Effective diameter of a circle having the same area as the sum of all the dust particles and nucleus.

^b Cross-section of all the dust particles.

^c Dust mass from Equation (7).

^d Dust production rate from Equation (8).

^e Dust production rate from Equation (10).

^f MJD 58786: UT 2019-10-30, inbound. $R_h=1.20$ au, $\Delta=0.40$ au, and $\alpha=49.8^\circ$.

^g MJD 58860: UT 2020-01-11/12, outbound. $R_h=1.01$ au, $\Delta=0.09$ au, and $\alpha=70.2^\circ$.

^h $Af\rho = 2.9\pm0.4$ cm from Equation (9).

ⁱ $Af\rho = 10.6\pm0.4$ cm from Equation (9).

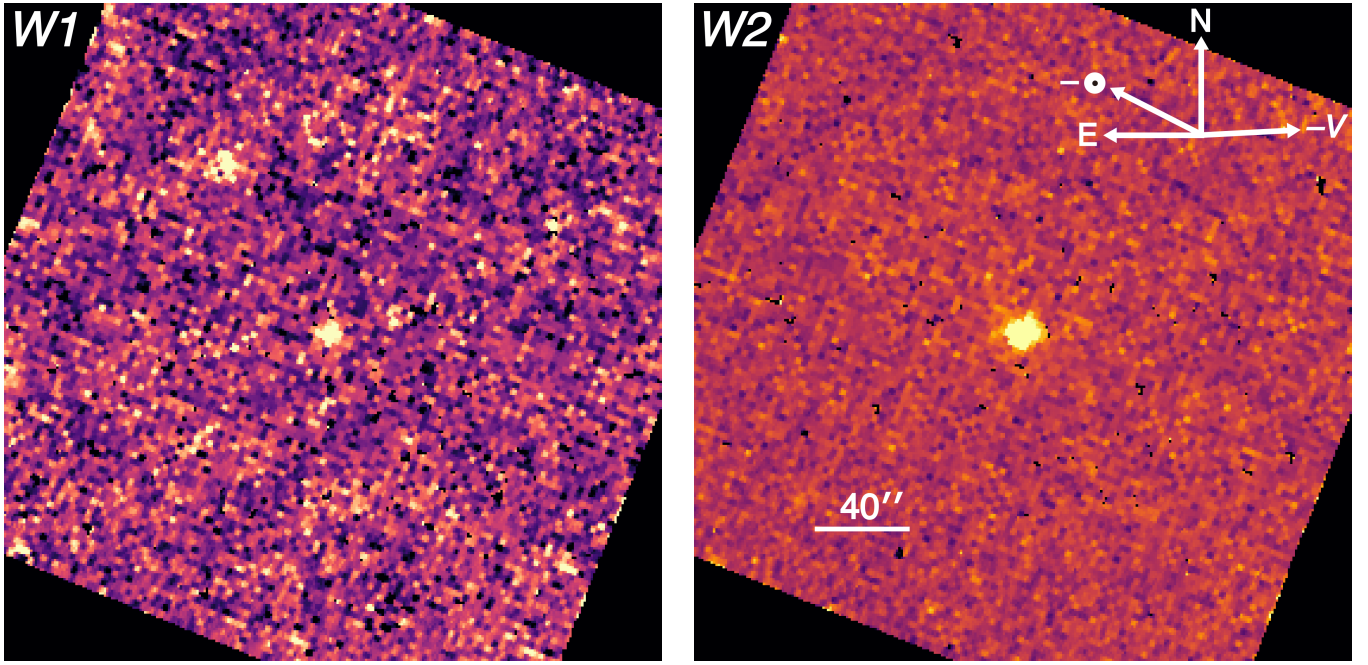


Figure 1. The ICORE coadded images of 289P (center) in Visit *A* (MJD 58786: UT 2019-10-30, inbound). Both frames have a size of $277'' \times 277''$. The left panel shows the *W1*-band image (38.5 seconds integration) with the FWHM $\theta_F = 7''.2$, while the right panel shows the *W2*-band image (46.2 seconds integration) with $\theta_F = 7''.7$. Heliocentric, *WISE*-centric distances and phase angle were $R_h = 1.20$ au, $\Delta = 0.40$ au and $\alpha = 49.8^\circ$, respectively. The cardinal directions (*N* and *E*), the direction of the negative heliocentric velocity vector ($-V$), and the anti-solar direction ($-\odot$) are marked. A $40''$ scale bar is also shown.

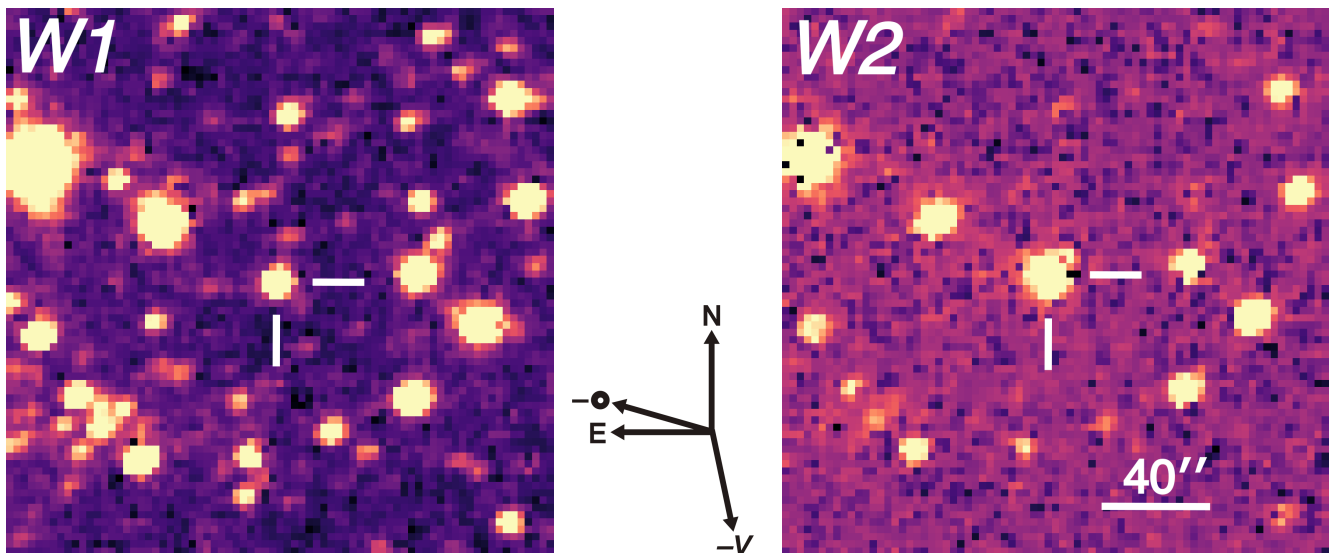


Figure 2. The median-combined images of 289P (center) in Visit *B* (MJD 58860: UT 2020-01-11/12, outbound). Both frames have a size of $200'' \times 200''$ with an integration time of 15.4 seconds. The left panel shows the *W1*-band image with the FWHM $\theta_F = 6''.6$, while the right panel shows the *W2*-band image with $\theta_F = 6''.9$. A $40''$ scale bar is included. $R_h = 1.01$ au, $\Delta = 0.09$ au and $\alpha = 70.2^\circ$. *N* and *E* exhibit the cardinal directions. $-V$ shows the direction of the negative heliocentric velocity vector and $-\odot$ shows the anti-solar direction, respectively.

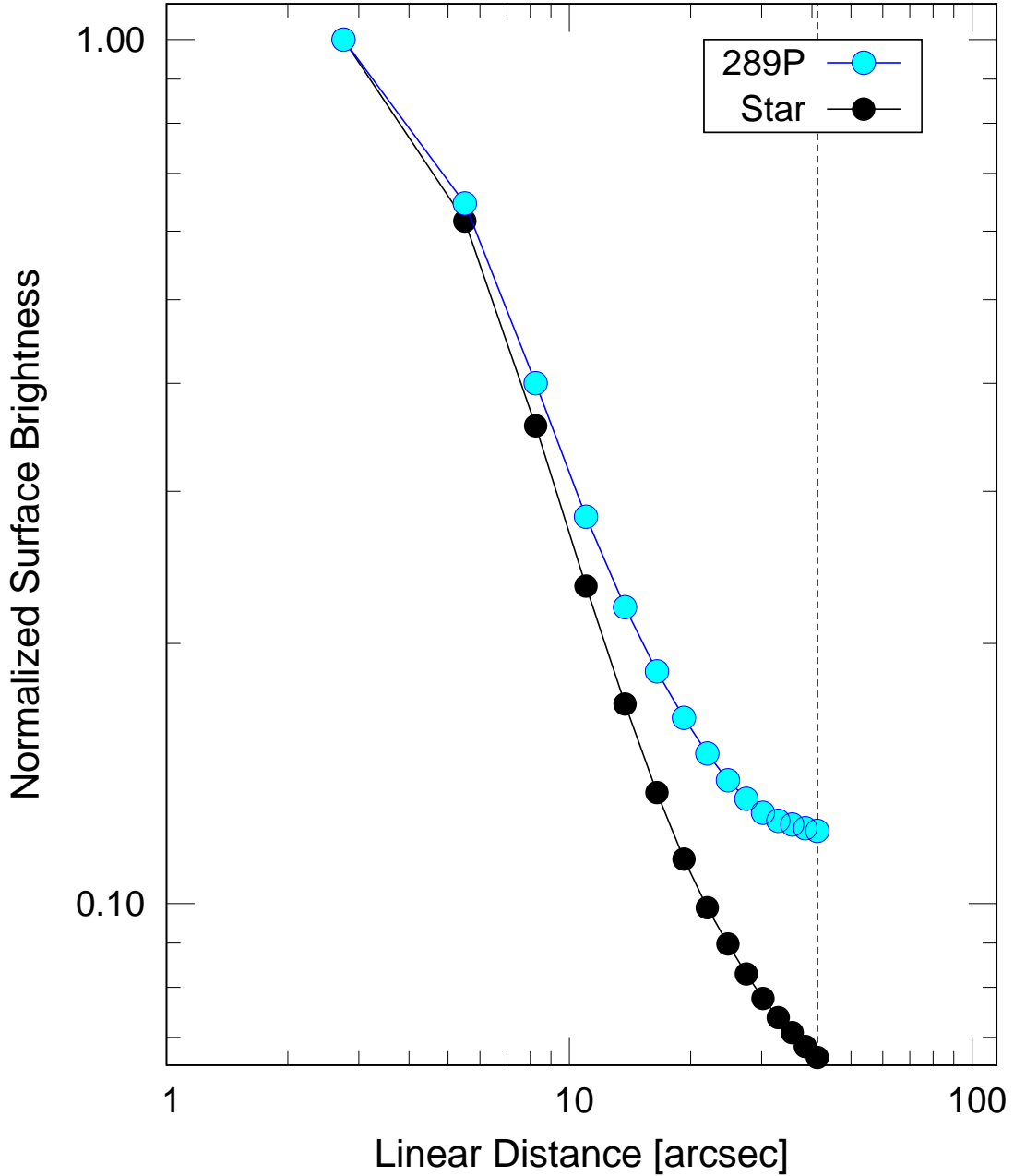


Figure 3. Normalized surface brightness profiles of 289P (blue circles) and a field star (black circles), from median-combined *W1* image in Visit *B* (MJD 58860: UT 2020-01-11/12, outbound) (Figure 2, left panel). The FWHM of 289P is $\theta_F = 6''.6$. The linear distance $> 40''$ is precluded (vertical dashed line) due to the nonuniform background, preventing further profile analysis.

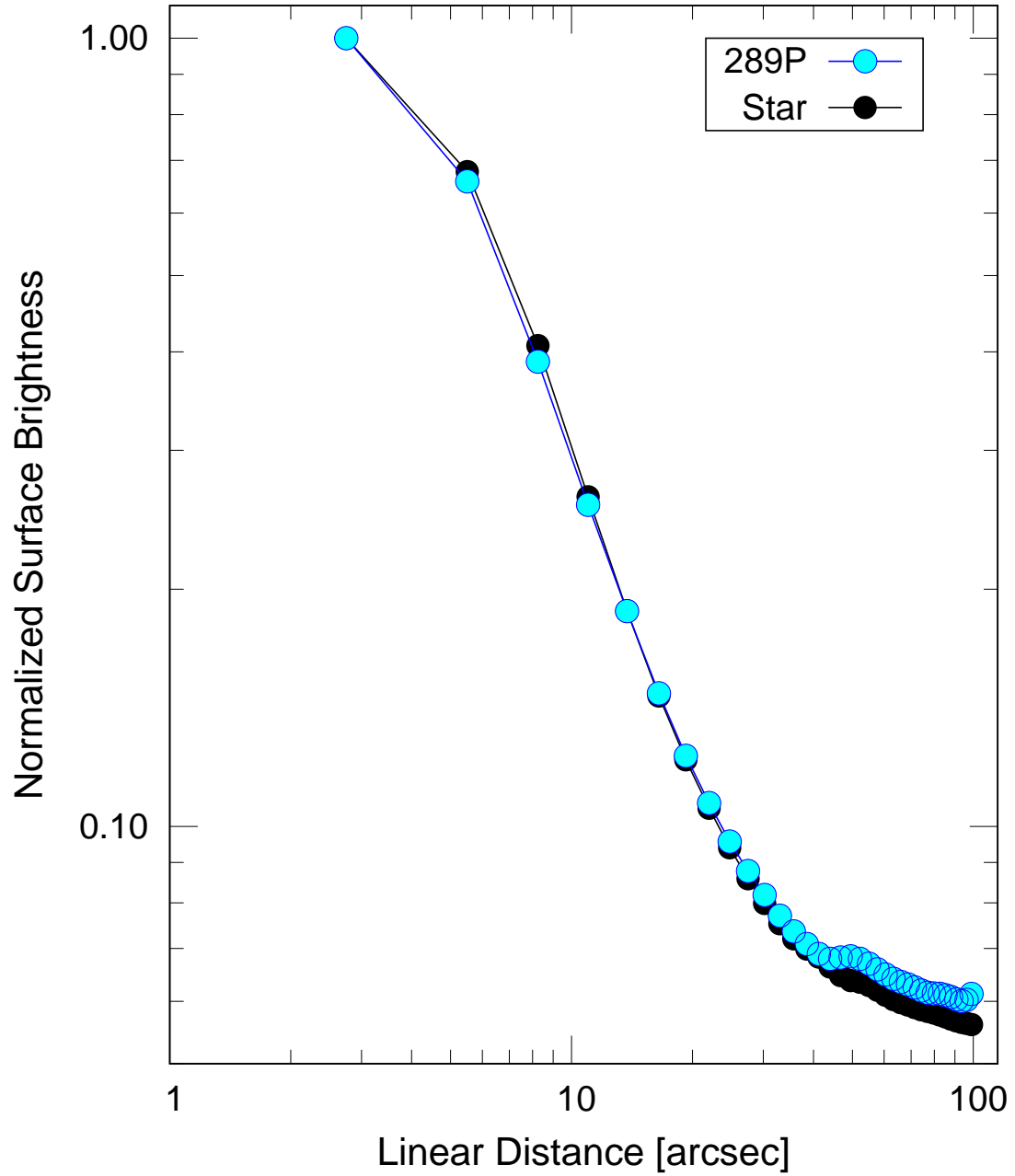


Figure 4. Same as Figure 3, but from the $W2$ -band from Figure 2, right panel. The FWHM of 289P is $\theta_F = 6''.9$.

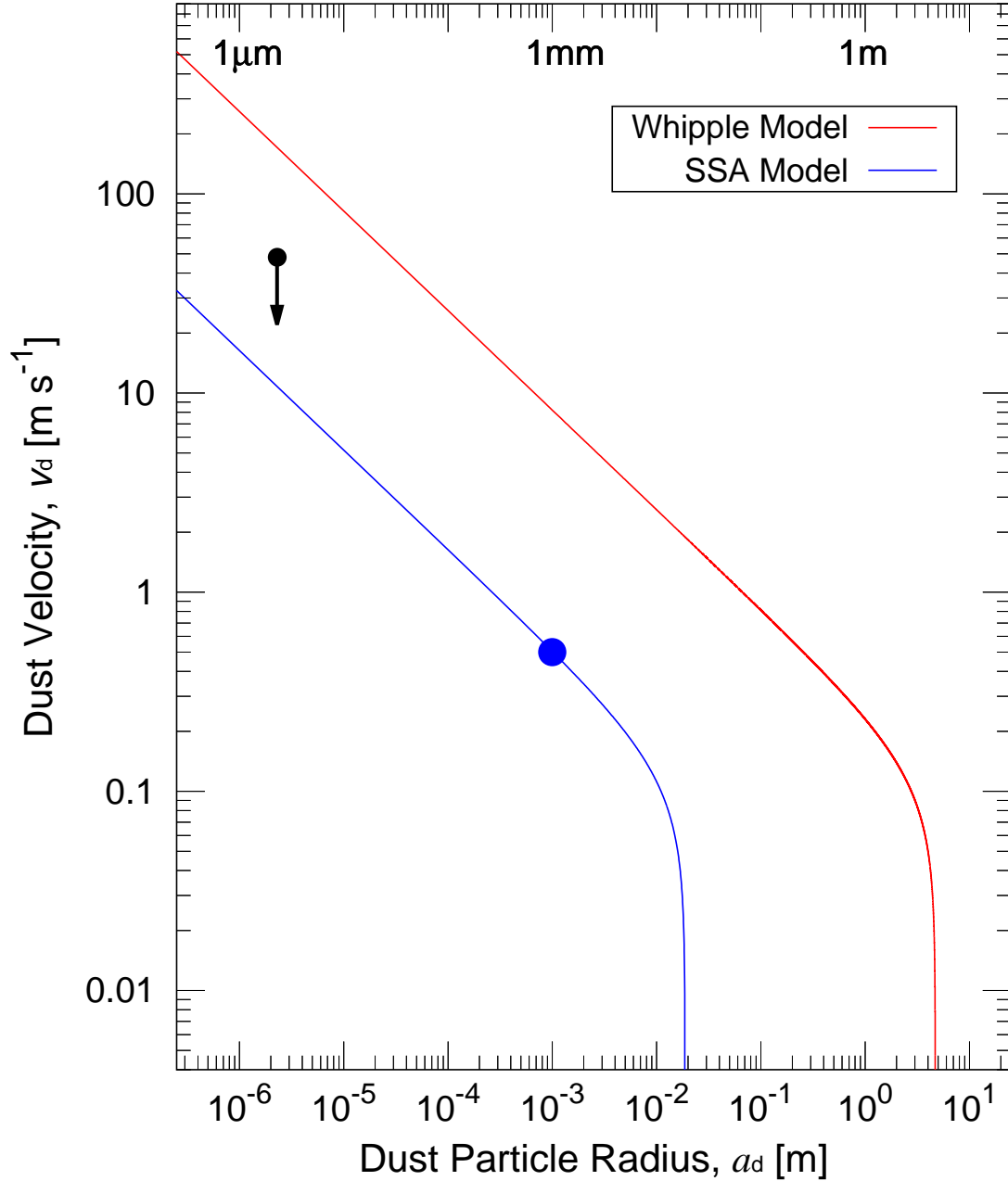


Figure 5. Models of the ejection velocity of dust from 289P as a function of particle radius. The SSA model (blue curve) and the Whipple model (red curve) are compared. The blue circle marks the particle radius $a_d = 1$ mm and the velocity $v_d = 0.5$ m s^{-1} determined by the 1956 Phoenicids researches (Section 3.2). The black symbol indicates $a_d = 2.3$ μm and $v_d < 48$ m s^{-1} limited by the FWHM of 289P in the $W2$ band (Section 3.1).

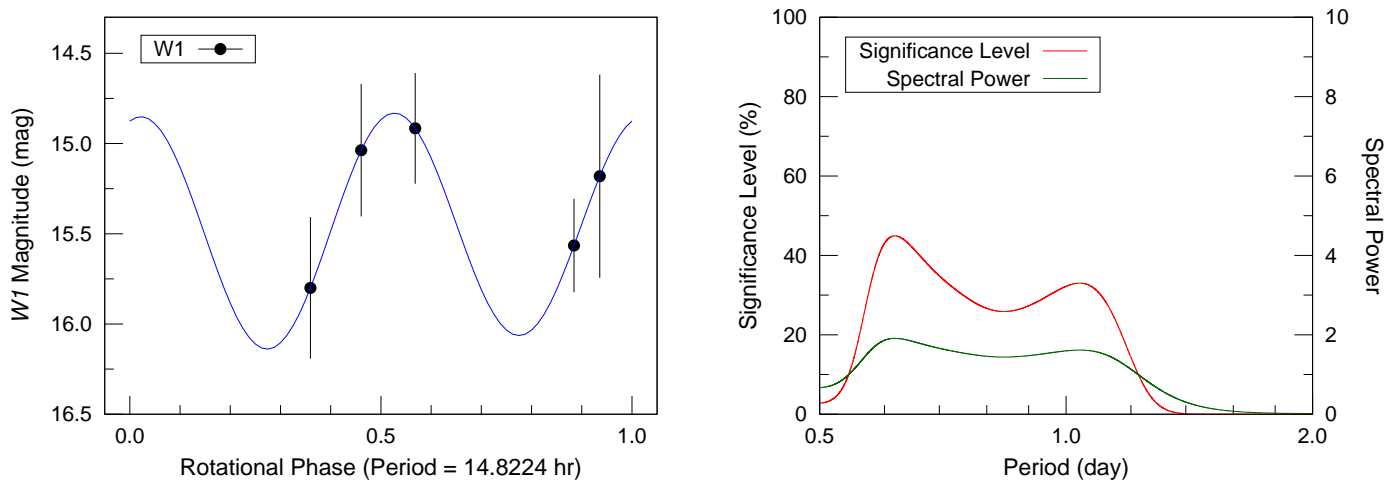


Figure 6. The left panel shows *W1*-band photometry of 289P in Visit *A* (MJD 58786: UT 2019-10-30, inbound), phased to the two-peaked period $P_{\text{rot}} = 14.8224 \pm 2.9899$ hr $\approx 15 \pm 3$ hr. The blue curve displays fitting result having amplitude ~ 1.3 mag. The right panel shows spectral analysis curves for the data. The maxima at $P_{\text{rot}} = 0.6176$ day ($= 14.8224$ hr) is taken as the best solution. The significance level is $\sim 45\%$.

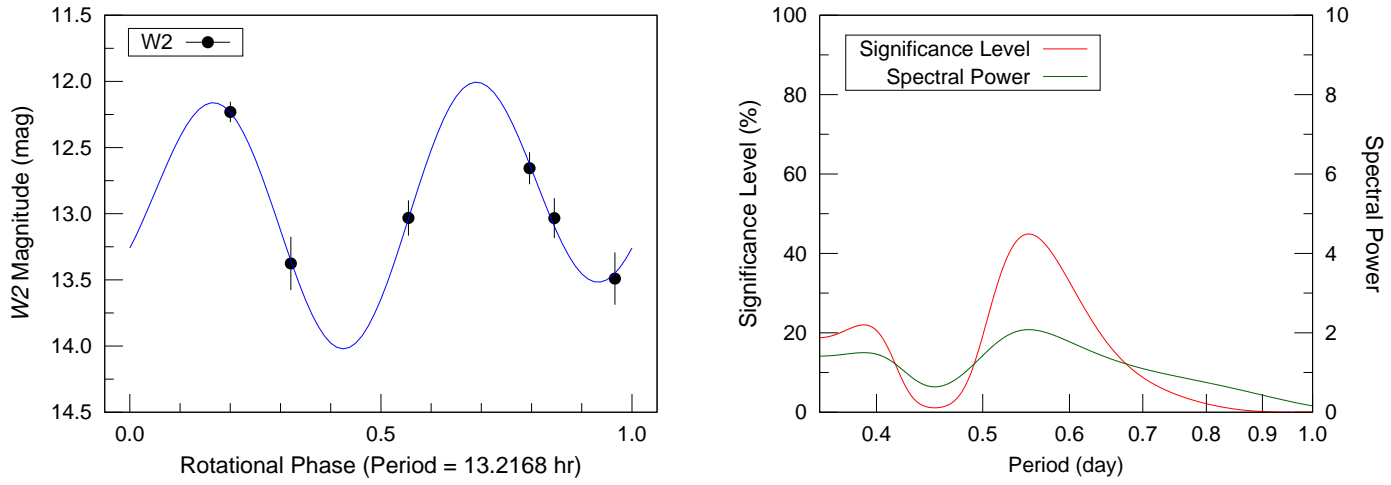


Figure 7. Same as Figure 6 but from the $W2$ -band, presenting the $P_{\text{rot}} = 13.2168 \pm 2.3551$ hr $\approx 13 \pm 2$ hr with an amplitude ~ 2.0 mag in the left panel and the maxima $P_{\text{rot}} = 0.5507$ day ($= 13.2168$ hr) in the right panel. The significance level is $\sim 45\%$.

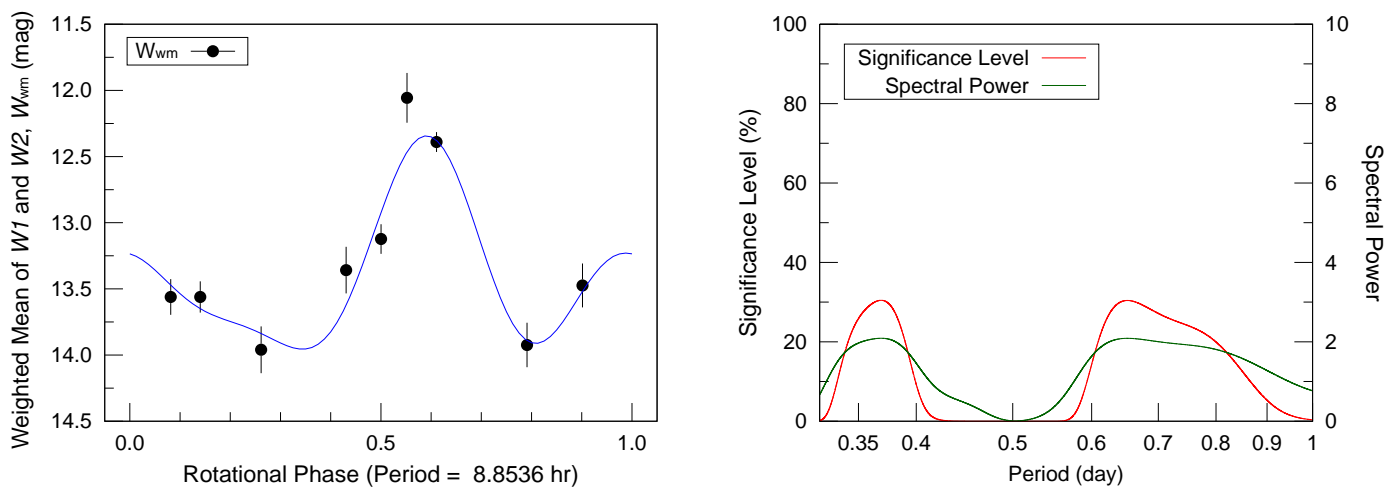


Figure 8. Same as Figure 6 but from the weighted mean of $W1$ and $W2$ magnitudes (W_{wm}), presenting the $P_{rot} = 8.8536 \pm 0.3860$ hr with an amplitude ~ 1.6 mag in the left panel and the maxima $P_{rot} = 0.3689$ day ($= 8.8536$ hr) with a significance level of 30.5% in the right panel. Another candidate $P_{rot} \sim 15.6$ hr (~ 0.65 day) has a significance level of 30.4%.

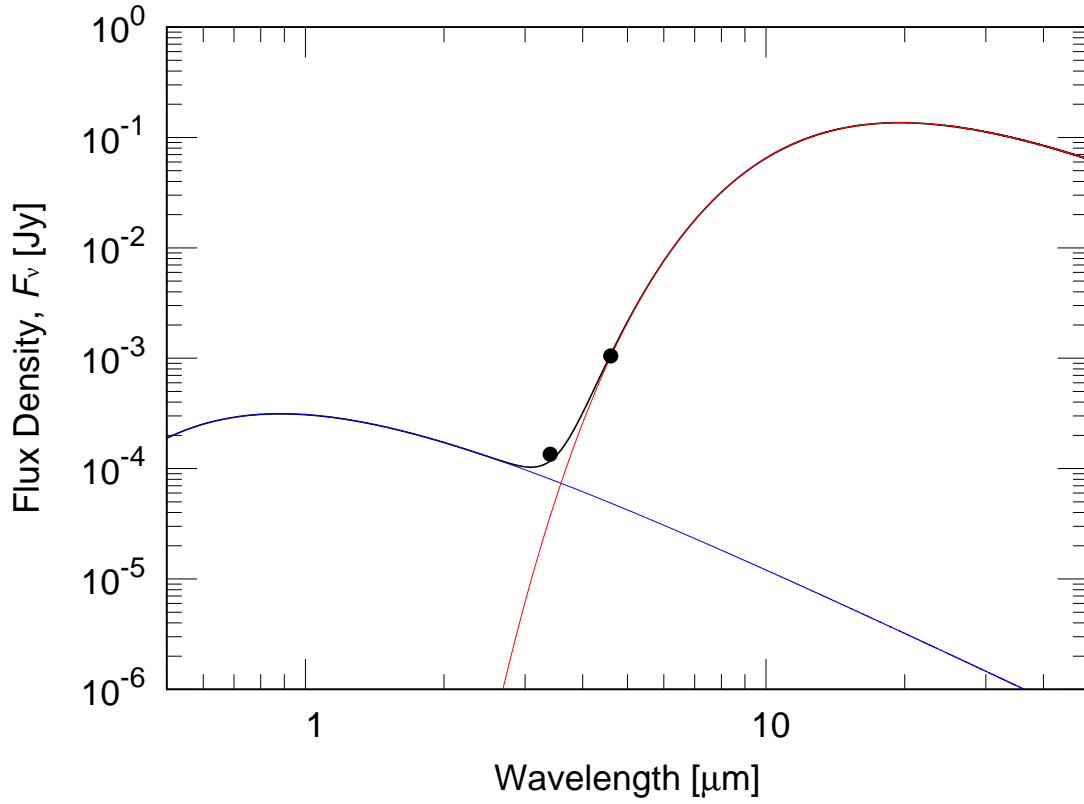


Figure 9. Calculated spectral energy distribution and measured flux densities from the 289P composite image in Visit A (MJD 58786: UT 2019-10-30, inbound). The flux densities at $W1$ ($3.4\mu\text{m}$) and $W2$ ($4.6\mu\text{m}$) are shown as points. The uncertainties are within the point size. The reflected sunlight model (blue line), thermal model (red line) and combined signal (black line) are over-plotted. The geometry, $R_h=1.20$ au, $\Delta=0.40$ au, and $\alpha=49.8^\circ$, are used for the models.

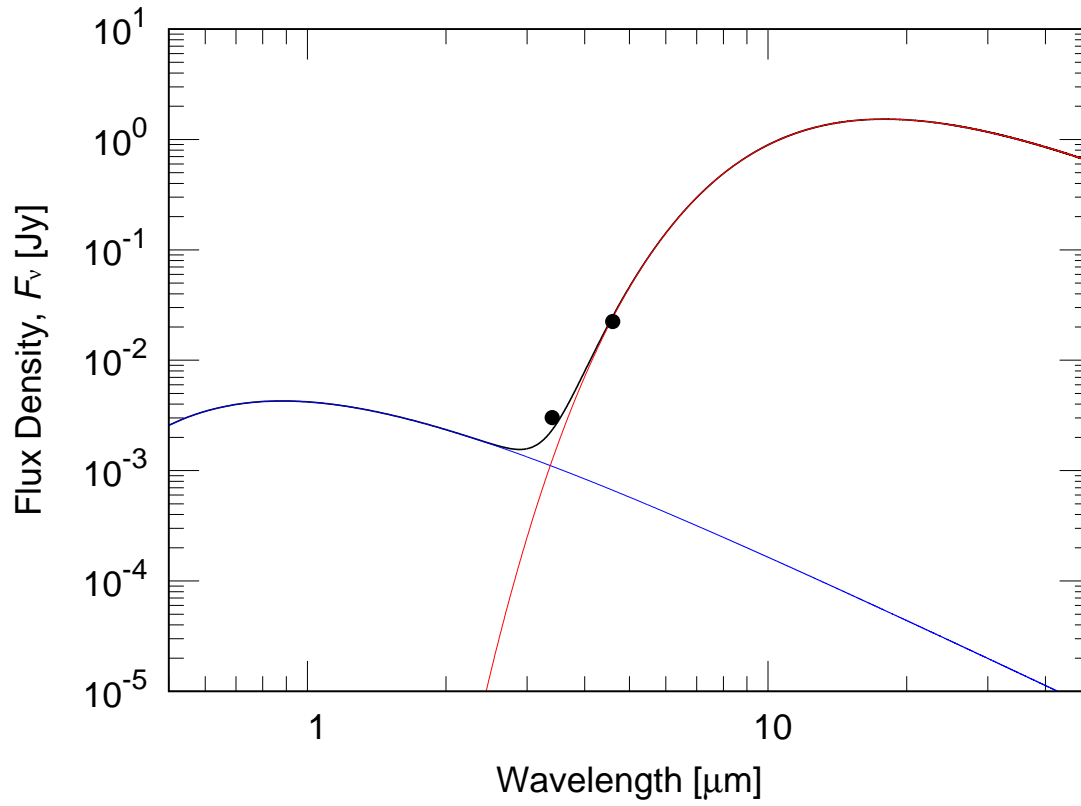


Figure 10. Same as Figure 9 but in Visit *B* (MJD 58860: UT 2020-01-11/12, outbound). $R_{\text{h}}=1.01$ au, $\Delta=0.09$ au, and $\alpha=70.2^\circ$ are used for the models.

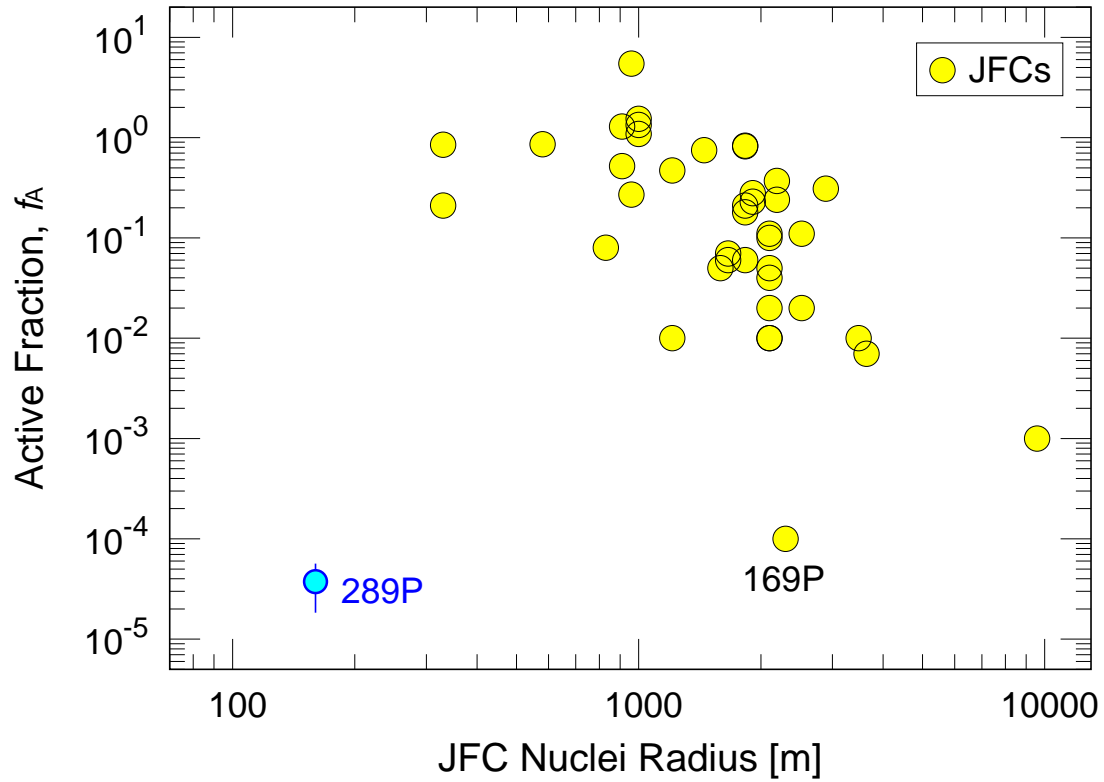


Figure 11. Relationship between JFC nuclei radius and fractional active area, f_A . The f_A of 289P is estimated near its perihelion, despite being among the lowest in JFCs, comparable to the inactive state of 169P.

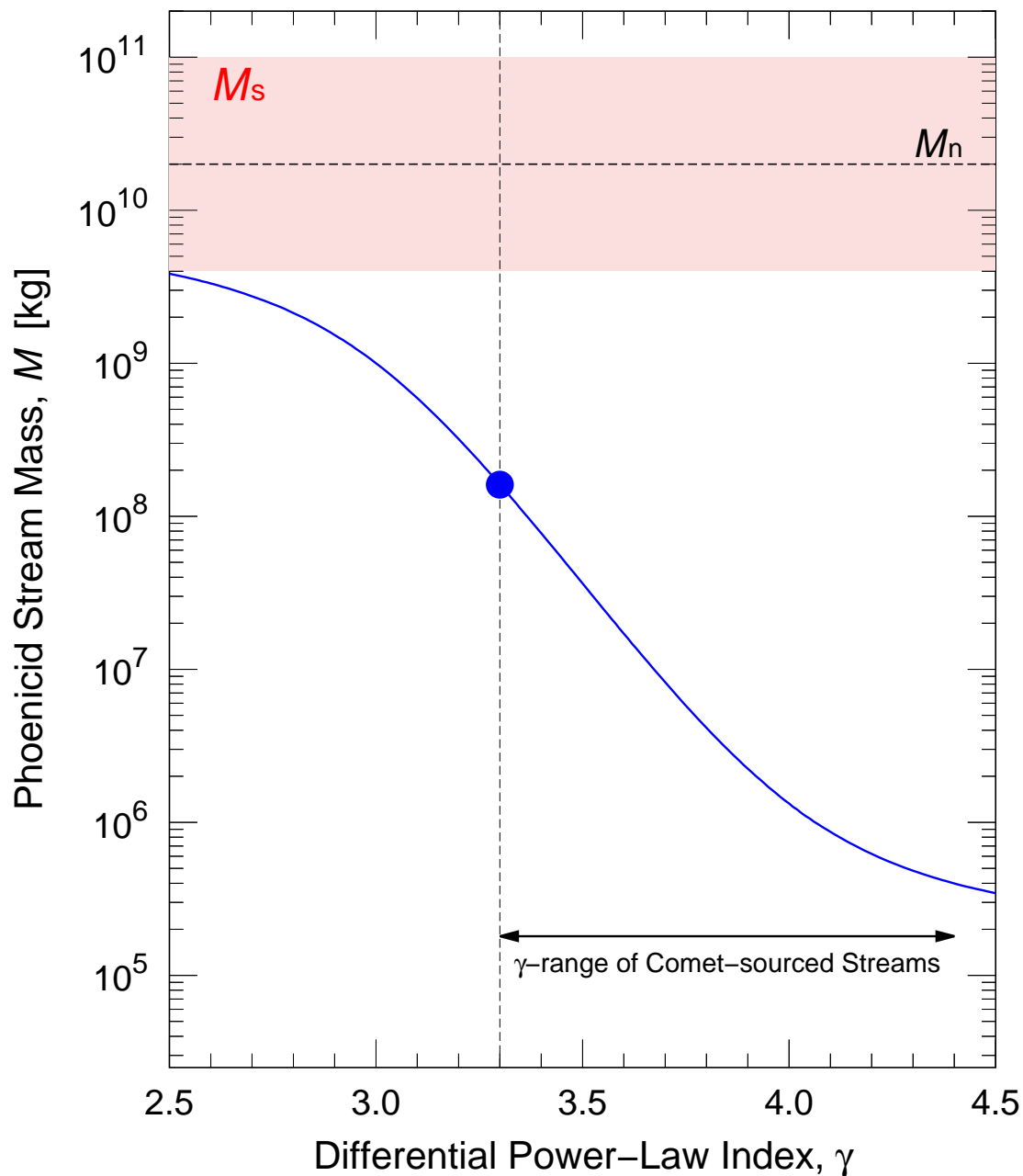


Figure 12. Phoenicid stream mass is plotted as a function of the differential power-law index, γ , as a blue solid line ($\gamma \neq 3.0, 4.0$ in Equation (13)). The possible stream mass range (M_s), based on the nucleus mass (M_n , Jewitt 2006) and the estimated stream mass ($\sim 10^{11}$ kg, Jenniskens & Lyytinen 2005), is shown as a reddish horizontal band. The Phoenicid stream mass is determined at $\gamma = 3.3$ (blue circle), which lies closest to the possible stream mass range, within the plausible index range $3.3 \leq \gamma \leq 4.4$ (double-headed arrow) derived from the observed comet-sourced meteoroids (Blaauw et al. 2011; Egal et al. 2022a,b; Koten et al. 2023; Moorhead et al. 2024).

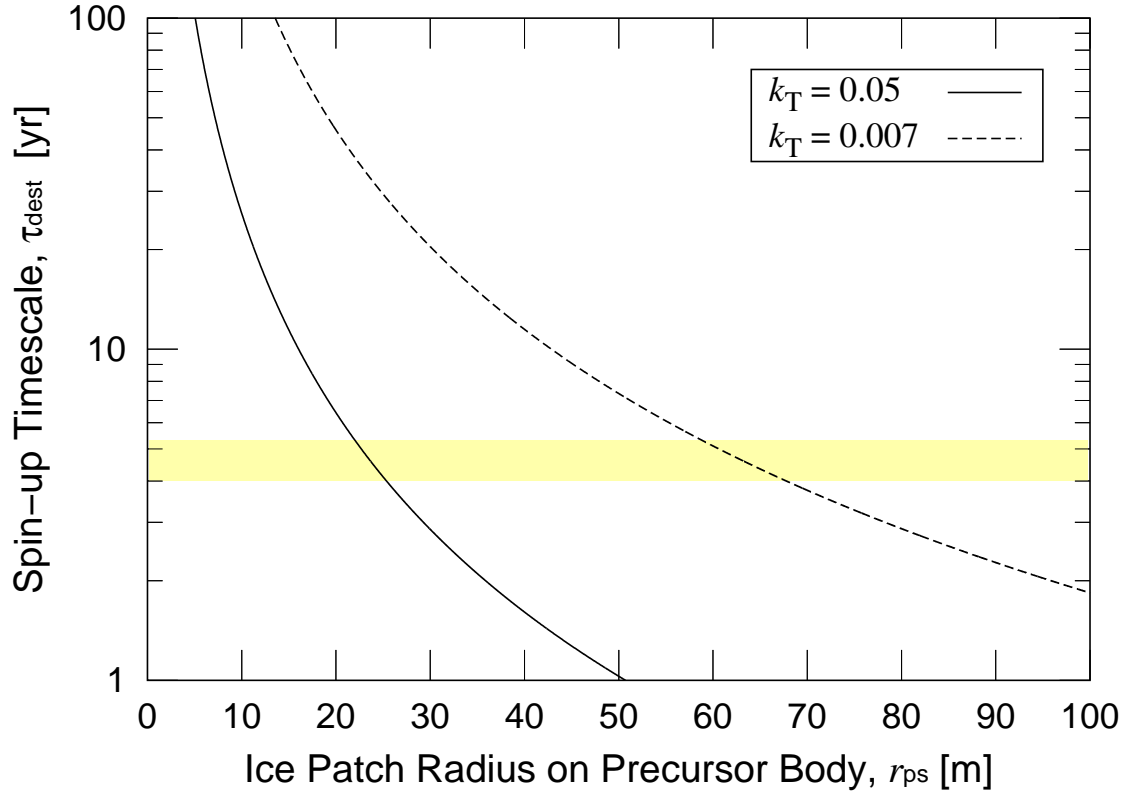


Figure 13. Precursor spin-up timescale is plotted as a function of radius of ice sublimating area (patch), r_{ps} , from Equation (15). Solid and dashed curves (black) show $k_T = 0.05$ and 0.007 (Jewitt 1997, 2021), respectively. A horizontal band (yellow) indicates the range of spin-up timescales constrained both by orbital period and empirical observations. The two curves within the band highlight the parameter space where rotational destruction can occur.

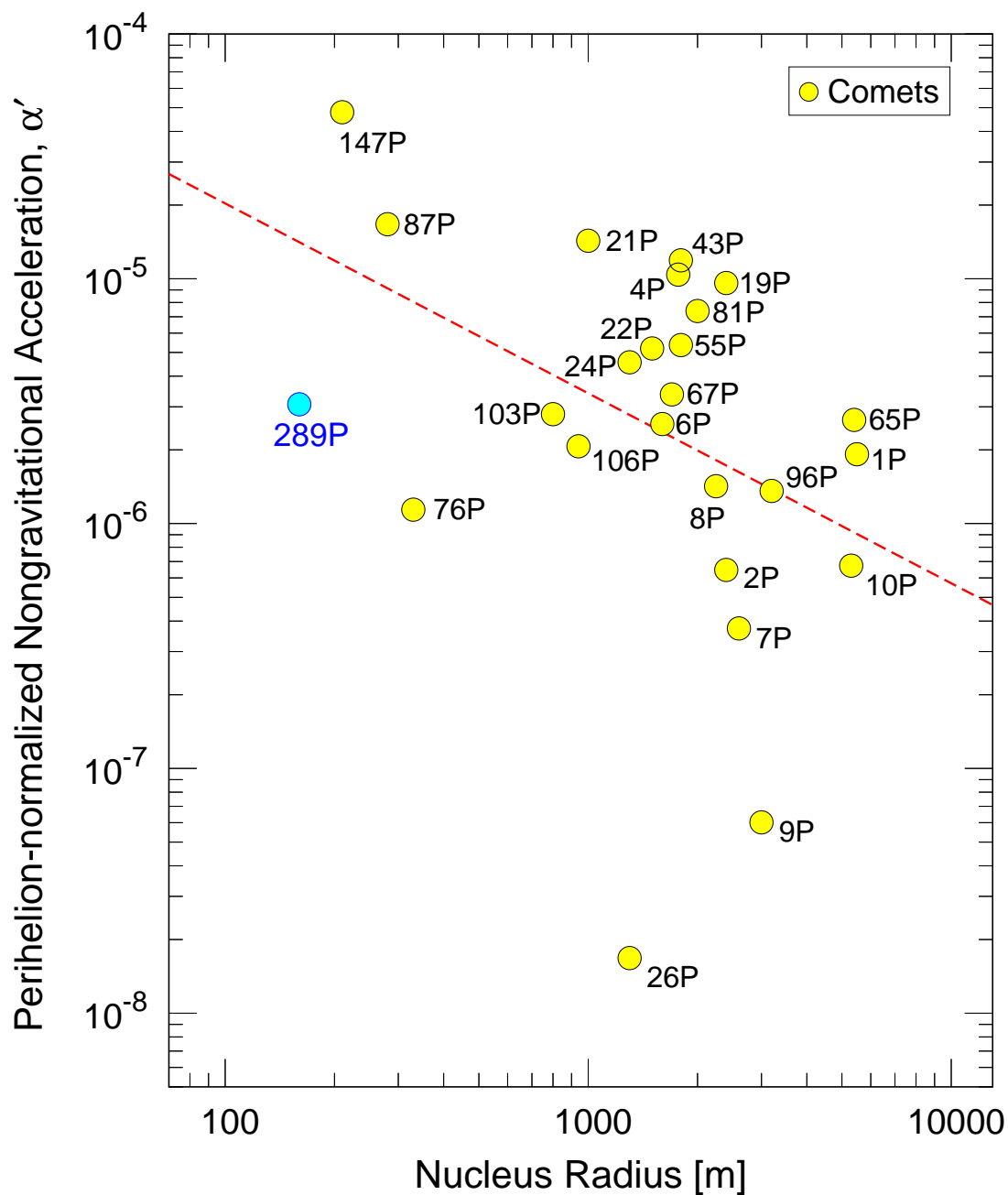


Figure 14. Nucleus radius versus perihelion-normalized nongravitational acceleration of 289P (blue symbol) and comparison with those of well-studied short period comets (yellow symbols). The dashed red line indicates the trend found by fitting from the latter data, which is Halley-type (1P and 55P), Encke-type (2P, 87P, and 147P), and JFCs (4P, 6P, 7P, 8P, 9P, 10P, 19P, 21P, 22P, 24P, 26P, 43P, 65P, 67P, 76P, 81P, 96P, 103P, and 106P).